THESIS

FLOW, SEDIMENT TRANSPORT, AND BED TOPOGRAPHY IN STRAIGHT AND

CURVED GRAVEL-BED CHANNELS

Submitted by

Tessa Catherine Hanson

Department of Civil and Environmental Engineering

ABSTRACT

FLOW, SEDIMENT TRANSPORT, AND BED TOPOGRAPHY IN STRAIGHT AND

CURVED GRAVEL-BED CHANNELS

In recent years, many river restoration projects have aimed to restore natural channel

stability and dynamism by re-establishing channel meanders lost to historical channelization. An

understanding of meandering channel behavior is crucial to successful restoration of these rivers.

Meandering and straight channels differ greatly in terms of sediment transport, velocity, and

flow patterns under equilibrium conditions. The primary objective of this study was to

investigate the mechanisms responsible for sorting patterns in mixed-grain straight and curved

channels using flume experiments. After an absence of sorting was observed in the flume

experiments, the study objective was modified to: 1) investigate the formation, behavior, and

dynamics of free and forced bars within a straight channel with and without an upstream barrier

and 2) explore the mechanism that accommodates for spatial boundary shear stress variations in

curved gravel bed channels.

The flume experiments involved detailed measurements of bed topography, velocity, and

sediment transport in both a curved channel and straight channel with and without an upstream

obstruction. It was expected that the gravel bed meandering river would compensate for spatial

variability in boundary shear stress through surface grain size adjustment (sorting), as opposed to

sediment transport convergence. Instead, the data reveal sediment transport divergence as the

primary mechanism for balancing shear stress variability. The lack of sorting may likely be

attributed to low excess shear stress and steady, rather than unsteady flow conditions. Regarding

free and forced bar behavior, no stability was achieved in the straight channel without an obstruction. This can be attributed to a range of factors related to upstream boundary conditions, shear stress, and lack of forcing topography. It is suggested that future studies utilize both higher excess shear stress and unsteady flow conditions in investigating shear stress variability in curved gravel-bed channels.

ACKNOWLEDGEMENTS

TABLE OF CONTENTS

LIST OF TABLES

LIST OF FIGURES

1. INTRODUCTION

For the past 150 years, river engineers and other water resource managers have altered rivers, primarily in the form of channelization. Recent river restoration projects have aimed to restore channel complexity and natural dynamic channel stability through the reestablishment of alternate bars and channel meanders. An understanding of steady and unsteady flow patterns, in addition to morphological trends in topography, sorting, and sediment transport is crucial to effective river engineering.

Analytical theory has shown that alternate bars in straight channels emerge from a flat bed due to a morphodynamic instability where small perturbations in the bed topography induce perturbations in the flow and sediment transport fields that grow with time, provided the width-to-depth ratio and average driving stress are high enough (Blondeaux and Seminara, 1985; Colombini et al., 1987). Because these bars freely form and migrate downstream, they have been referred to as "free bars" (e.g., Tubino and Seminara, 1990; Seminara, 1998, Whiting and Dietrich, 1993).

Prior to 1981, the prevailing idea in the geomorphologic community about river meander formation was that this initial formation of alternate bars in a straight channel leads to alternating sequences of scour and deposition, causing localized areas of bank erosion which could progressively transform the channel into a meandering planform (Leopold and Wolman, 1960). More recently, however, it has been shown that meander formation is driven by bank erosion resulting from perturbations along the channel banks (the so-called "bend theory"; e.g., Ikeda et al., 1981; Blondeaux and Seminara, 1985; Johannesson and Parker, 1989), and the resonant

wavelength at which meanders form corresponds to the most unstable wavelength of alternate bar instability (Blondeaux and Seminara, 1985).

In meandering channels both the channel curvature and bed topography cause the boundary shear stress to be high toward the inside bank at the entrance to the bend and to be high in the pool at the downstream part of the bend. This methodical shifting of the maximum boundary shear stress from inner towards outer bank encourages the deposition on the inner bank, producing point bars (Dietrich and Smith, 1984). Because these features are forced by the channel curvature, they are sometimes referred to as "forced bars" (e.g., Tubino and Seminara, 1990; Seminara and Solari, 1998, Whiting and Dietrich, 1993). Forced bars can also arise due to flow obstructions (Thompson and McCarrick, 2010; Nelson et al., 2010), which create a combination of backwater and flow convergence (jet flow) resulting in increased flow velocities past the barrier and a recirculating eddy directly downstream, causing deposition downstream of the obstruction.

While forced and free bars can coexist in meandering channels, it has been found that many channels may have a threshold curvature where migrating bars are suppressed (Blondeaux and Seminara, 1984; Tubino and Seminara, 1990; Whiting and Dietrich, 1993), especially with the increase of forced bars (Kinoshita and Miwa, 1974). Overall, free bar formation and movement in meandering channels is affected by degree of curvature, planform geometry, and width-to-depth ratio (Whiting and Dietrich, 1993). Free bars become less able to migrate in curved channels as the width-to-depth ratio increases (Garcia and Nino, 1993; Whiting and Dietrich, 1993). Bar migration typically occurs in lower amplitude bends and straight channels (Whiting and Dietrich, 1993). Both bar height and migration speed are smaller in meandering channels than in straight ones (Garcia and Nino, 1993).

One of the feedbacks between bedforms and sediment transport in meandering channels is related to the components of secondary flow, which are induced by channel curvature (Seminara, 2006). Through the bend of a meander, the flow experiences a centrifugal force, along with a counteracting pressure force (Seminara, 2006; Bridge and Jarvis, 1982; Ikeda,1989). These forces lead to both superelevation and secondary circulation where flow near the bed is directed toward the inner bank and flow at the water surface is directed toward the outer bank (Dietrich and Smith, 1983; Dietrich and Whiting, 1989).

This secondary circulation can have important consequences for bed surface sorting patterns. Meandering streams with heterogeneous sediment loads move different grain sizes in different proportions and directions (Parker and Andrews, 1985). The force of the near-bed secondary circulation felt by particles on the point bar at the inner bank of a bend is counteracted by the gravitational force provided by the cross-stream slope of the point bar, and coarse particles will tend to roll downhill into the pool while fine particles will be pushed up the bar by the near-bed flow (Parker and Andrews, 1985; Ikeda, 1989, Clayton and Pitlick, 2007). This results in bed surface sorting patterns in channel bends with fine bars and coarse pools (e.g., Bluck, 1971; Bridge and Jarvis, 1976, 1982; Bluck, 1987; Whiting and Dietrich, 1991; Laronne and Duncan, 1992; Carson, 1986; Clayton and Pitlick, 2008; Clayton 2010). Conversely, the opposite sorting pattern of coarse bars and fine pools tends to be observed in straight channels with alternate bars (e.g., Mosley and Tindale, 1985; Kinerson, 1990; Lisle and Hilton, 1992; Lisle and Madej, 1992). Flume experiments (Nelson et al., 2010) and numerical modeling studies (Nelson et al., 2015a, 2015b) suggest that this pattern of coarse bar tops and fine pools in straight channels is the result of interactions between spatially-varying boundary shear stress and the selective nature of lateral (cross-stream) bedload transport.

Field studies at Muddy Creek, Wyoming, have documented the relationship between flow, sediment transport, and bed topography in a sand-bedded meander (Dietrich and Smith 1983, 1984; Dietrich and Whiting, 1989). The channel curvature and bar-pool topography causes a zone of maximum boundary shear stress to shift from the bar on the inner bank to the pool on the outside of the bend. Their measurements of sediment transport and bed surface grain size indicated that at equilibrium this spatial variation in shear stress is accommodated by both cross-stream bedload transport and changes in bed surface grain size. To investigate whether this was also the case for gravel-bedded meanders, Dietrich and Whiting (1989) presented measurements of flow and sediment transport collected in a tributary of the Rio Grande del Rancho River. These observations were somewhat coarse, however, and the boundary shear stress declined sharply in the downstream direction, which caused sand to drop out of suspension, travel as bedload, and make the bar finer. Nevertheless, they speculated that cross-stream variation in grain size in gravel-bed meanders may exert a larger control on bedload transport and equilibrium bed topography than in sand-bedded bends. I am not aware of any field or flume studies in gravel-bed meanders where simultaneous measurements of flow, sediment transport, and bed topography have been collected under steady flow conditions.

The initial objective of this research was to conduct flume experiments in straight and curved gravel-bed channels to develop coarse bars and fine pools in the straight channel and fine bars and coarse pools in a curved channel, to make detailed measurements of bed topography, the flow field, and the sediment transport field to identify mechanisms responsible for the different sorting patterns. During the course of the experiments, however, the expected sorting patterns did not develop. I therefore modified my objectives to: 1) investigate free and forced bar formation, behavior, and dynamics in a straight channel with and without an obstruction and 2)

to measure flow, bed topography, bed surface sorting, and sediment transport under equilibrium conditions in a curved gravel-bed channel to explore the extent to which surface grain size variability and sediment transport divergence accommodate spatial variations in boundary shear stress.

2. METHODS

2.1 Experimental setup

I conducted three experimental runs, two in a straight flume and one in a curved flume. Run 1 was conducted in the straight flume with no obstruction, Run 2 was conducted in the straight flume with an upstream obstruction, and Run 3 was conducted in the curved flume with no obstruction. The upstream barrier in Run 2 was a piece of sheet metal that spanned approximately 1/3 of the channel width (0.5 m). Both the straight and curved flumes were constructed in a 4.88 m wide, 15.2 m long basin at Colorado State University's Engineering Research Center Hydraulics Lab (Daryl B. Simons Building). The flume walls were constructed with wood 2 x 4's and sheet metal, to create a smooth boundary surface. Both flumes occupied the entire 15.2 m length of the basin, and both had a constant width of 1.35 m. The curved channel was designed as a sine-generated curve (Langbein and Leopold, 1966), where the flume centerline is described by:

$$\phi = \omega sin \frac{2\pi s}{M}$$

where ϕ is the angular deviation of the centerline from the down-valley axis at a distance s downstream along the channel centerline, M is the meander wavelength, and ω is the angle between the centerline and down-valley axis at the crossing between the bends. The crossing is defined as the segment of channel between the bends where the radius of curvature is infinite. The curved flume was constructed to have a crossing angle (ω) of 20° and it contained a single wavelength (M) of 12.2 m. The two flumes are shown in Figure 1.

Figure 1. The Straight (0 degree) channel configuration (top) and meandering channel (bottom) seen from the downstream end. Note the sediment feeder located at the head of the channels and the targets placed in equal increments on the walls.

The sediment mixture used in the experiments ranged from 1 to 8 mm, with a median grain size (D_{50}) of 4 mm and a geometric standard deviation (σ_g) of 1.60 (Figure 2).
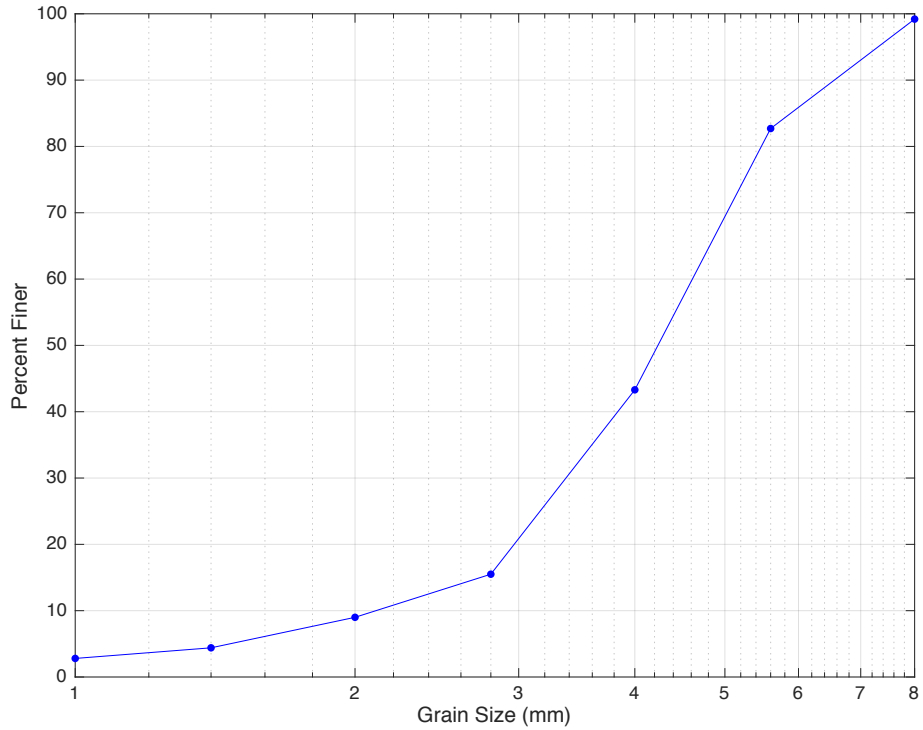
Figure 2. Experimental grain size distribution.

This range of sizes was selected so that sorting patterns on the bed would be observable. Sediment was supplied to the flume at the upstream end with a variable-speed auger-type sediment feeder, and bedload exiting the flume was captured in a sediment trap that spanned the width of the flume.

Water was pumped from a sump underneath the floor of the laboratory to the upstream end of the flume, through a set of baffles to straighten the flow and reduce potential scour at the inlet. The water surface elevation at the downstream end of the flume was controlled by an adjustable tailgate located just downstream of the end of the sediment trap.

Targets were affixed to the walls in both channels (Figure 1). The targets were spaced about 0.3 m apart, and were located approximately 0.5 m above the bottom of the flume walls. The locations of these targets were acquired with a terrestrial laser scanner, and the targets were used to scale and register structure-from-motion topographic point clouds collected throughout the experiment (described in more detail below).

2.2 Experimental procedure

The overall procedure for the three runs was identical. The flume was filled with the bulk sediment mixture and screeded flat to an initial slope provided in Table 1. For both channels, I specified the water discharge and initial slope so that the width-to-depth ratio would be about 20 and the ratio of the mean dimensionless shear stress to the critical dimensionless shear stress would be about 2, so that all grain sizes would be mobile (Wilcock and McArdell, 1993). Prior experiments have indicated that these conditions encourage the formation of alternate bars (Lanzoni, 2000; Venditti et al., 2012).

Table 1: Initial Channel Conditions

Fixed Parameters	
Channel Length	15.2 m
Wavelength	12.2 m
Channel Width	1.35 m
Channel Slope	0.0068, 0.0047, 0.0053 m/m
Width to Depth Ratio	20
Crossing Angles	0,20
Mean Depth	0.0675 m
Target Transport Rate	59 kg/h
Median Grain Size (D50)	4 mm
Geometric Median Size (D_g)	3.87 mm
Geometric Standard Deviation (σ_g)	1.60

For all three experiments, sediment was supplied at a constant rate of 59 kg/h, calculated *a priori* with the Wilcock and Crowe (2003) algorithm for the grain-size distribution shown in Figure 2 and the shear stress estimated for the slopes and depths given in Table 1. Each experiment was run until equilibrium conditions were achieved. It was determined that the channel had reached equilibrium based on the weight of exiting sediment, the channel slope, and the movement of free bars within the channel. This resulted in total run times of 75 h for Run 1, 25 h for Run 2, and 40 h for Run 3. These times reflect the time to reach equilibrium. For each channel configuration, the flume was run for several more hours (typically five) while velocity (Runs 2 and 3) and bedload transport (Run 3) measurements were collected.

2.3 Measurements

During each experiment, the flume was periodically drained (generally in 5-hour increments) so that measurements of bed topography could be collected to document evolution of the bed. Under equilibrium conditions for Runs 2 and 3, an array of velocity and sediment transport measurements were collected along with photographs to document bed surface sorting patterns.

2.3.1 Topography

Bed topography was characterized using Structure-from-Motion (SfM). SfM is a method of photogrammetry that involves capturing multiple overlapping offset digital photographs that yield 3-D structures through reconstruction algorithms (Fonstad et al., 2013). SfM can yield very precise digital elevation models of surfaces with sets of images captured with a high degree of overlap. The digital photographs captured are uploaded into software that uses auto identification of matching features (i.e. targets) in overlapping images to reconstruct camera position and scene geometry (Westoby et al., 2012). Both the camera position and point coordinates are defined

iteratively through non-linear least-squares minimization (Westoby et al., 2012). This process yields an initial point cloud that is in an "image-space" coordinate system. To convert this to a more useful form ("object-space" coordinate system) a series of known ground-control are manually identified. These points are typically obtained via ground survey or LiDAR scan. Consumer grade digital cameras can be used effectively to achieve high resolution point clouds, however, one disadvantage of the method is long processing periods. SfM has been shown to produce topographic point clouds of greater resolution than and accuracy comparable to terrestrial laser scanners in a flume setting (Morgan et al., 2016).

In this experiment, an 18 megapixel (MP) Canon Rebel T3i camera with a 24 mm lens was mounted to a cart above the channel and used to capture the bed. Photographs were taken in one to 0.3 m intervals in the upstream and downstream directions, at a distance of 1.5 m (in the straight channel) and 1 m (in the curved channel) from the bed. The digital photos were processed (at "low" quality) using Agisoft PhotoScan Professional and the resulting point clouds were clipped and edited using CloudCompare. The point clouds were then interpolated using the nearest neighbor algorithm onto a 1 cm Surfer grid for processing in Matlab. The photo resolution was not scaled and though "low quality" point clouds were generated, the resulting point clouds still consist of $\sim 1.03 \times 10^6$ points on average (an average density of $\sim 5 \times 10^4$ points per m^2), which is more than satisfactory for observing topographical differences. The average error for identifying the control points in each photo was 0.006 m (the TLS (Terrestrial Laser Scanner) has an accuracy limit of 0.001 m). For both configurations, the channel was periodically (every 2-10 hours) drained and photos were taken of the bed to capture bed evolution, including the movement of free bars. Photos were also taken once equilibrium was reached with each configuration.

2.3.2 Water surface elevation

Water surface elevation measurements were collected periodically (every hour) throughout all of the runs using a meter stick and additionally, a point gage (when the velocity was collected). The measurements were collected 0.3 meters apart along the centerline of the channel.

2.3.3 Bed surface grain size

Bed surface grain size observations were collected in the form of photographs with the 18 MP Canon Rebel T3i camera. Digital photographs looking straight down onto the bed were taken at a distance of approximately 0.5 m above the bed over the grids described in Table 2 below. Photographs were taken of the dry bed of the curved and straight channels at the end of Runs 2 and 3. The photos were captured in a RAW format and processed with Canon Digital Photo Professional software to remove the lens distortion and export each image as a JPEG file. These images were then processed using the automated procedure described in Graham et al. (2005). This method uses a series of image processing techniques to identify individual grains in an image, and has been used successfully in similar gravel bed flume studies (Nelson et al. 2010; Bankert and Nelson, in review). After the image is converted to greyscale, a median filter is used to blur mineralogical speckles or other intragranular noise. A morphological bottom-hat filter is then used to enhance the photo contrast. The image is then thresholded twice by pixel intensity, where the first threshold identifies dark pixels that are possible grain edges, while the second threshold identifies the darkest pixels in the image which are almost certainly grain edges. A logical AND function is then used to merge the two thresholded images and identify the pixels that are most likely grain edges. A watershed transform is then applied to the classified image to segment the photograph into regions that represent likely sediment grains, and an h-minima

transform is applied to prevent over segmentation of larger particles. An ellipse is then fit to each

grain region and the minor axis is measured in pixels and converted to mm using the known

image scale. This generates an area-by-number grain size distribution, which is converted to a

grid-by-number (or equivalently volume-by-weight) distribution using the voidless cube model

(Kellerhals and Bray, 1976).

Table 2. Surface Grain Size Photo Grid

Run	Photos per cross section	Number of Photos [Total]	Length of Channel Captured [ft]
2	4	184	40
3	4	75	30

I selected values for the parameters used in this method by processing one of the

sediment images using all combinations of the parameters given in Table 3.

Table 3. Surface Grain Size Parameters

Parameter	Values Tested
Threshold 1	[20 25 30 **35** 40 45] %
Threshold 2	[**0.5** 1 1.5 2 2.5] %
Disk Radius	[3 4 5 6 **7**] pixels
Median Filter	[2 3 4 **5** 6 7] pixels
H_{min} Threshold	[0 **1** 2 3] pixel(s)

**The values used in the final analysis are given in bold.

The resulting D16, D50, and D84 estimated from each parameter combination were then

compared to those computed from a manual digital pebble count of the same image. To do this, a

10 x 10 grid was laid over the photograph in ArcGIS (see Figure 3) and polylines were traced

over the intermediate axis of each grain that fell directly underneath a grid intersection. The

polylines were measured in pixels, then converted to millimeters (mm) using the known scale.

The grain size distribution (CDF of the grain sizes) was obtained, in addition to key grain size

percentiles. The squared errors for each combination of parameters were summed and minimized to find the best fit. See Figure 4 for a comparison between the manually measured and automated grain size distributions. A comparison between the photo overlay and original photo is shown in Figure 5. The error associated with the automated image analysis was estimated to be approximately 2 mm.
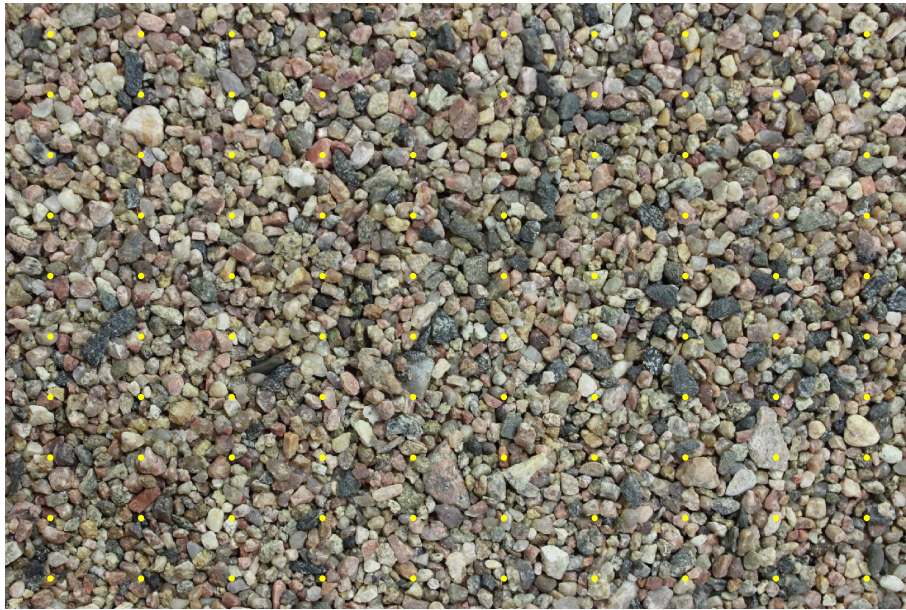

Figure 3. Calibration photo and fitted grid (100 nodes).
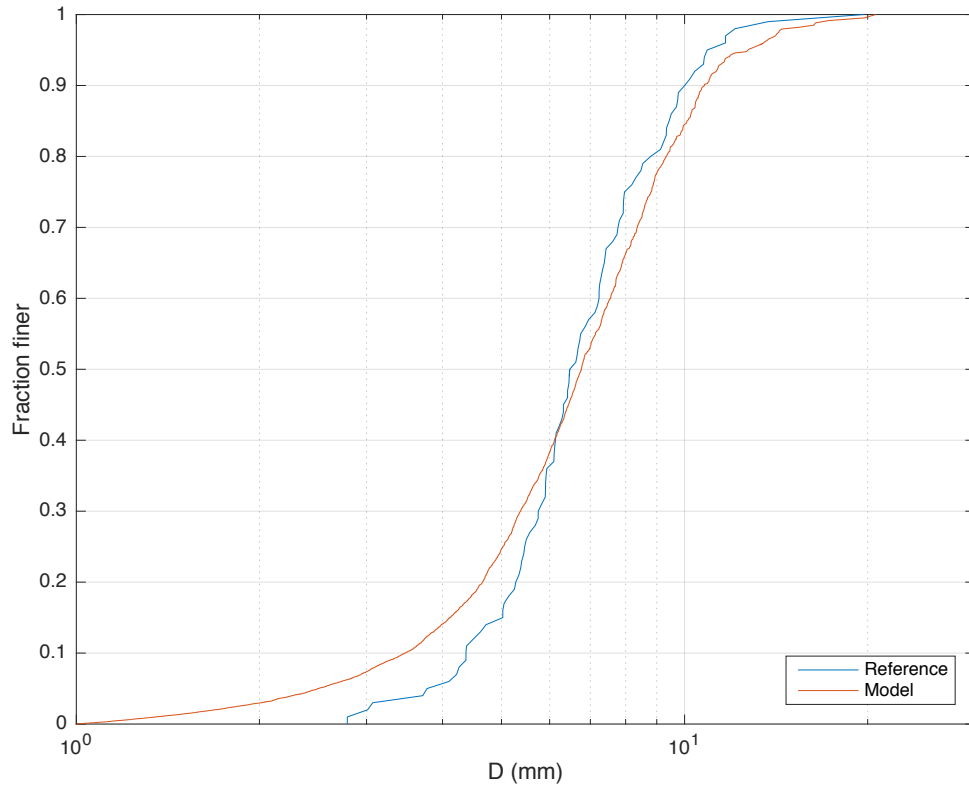
Figure 4. Grain size distributions yielded from the validation process ("Reference") and model calibration ("Model").
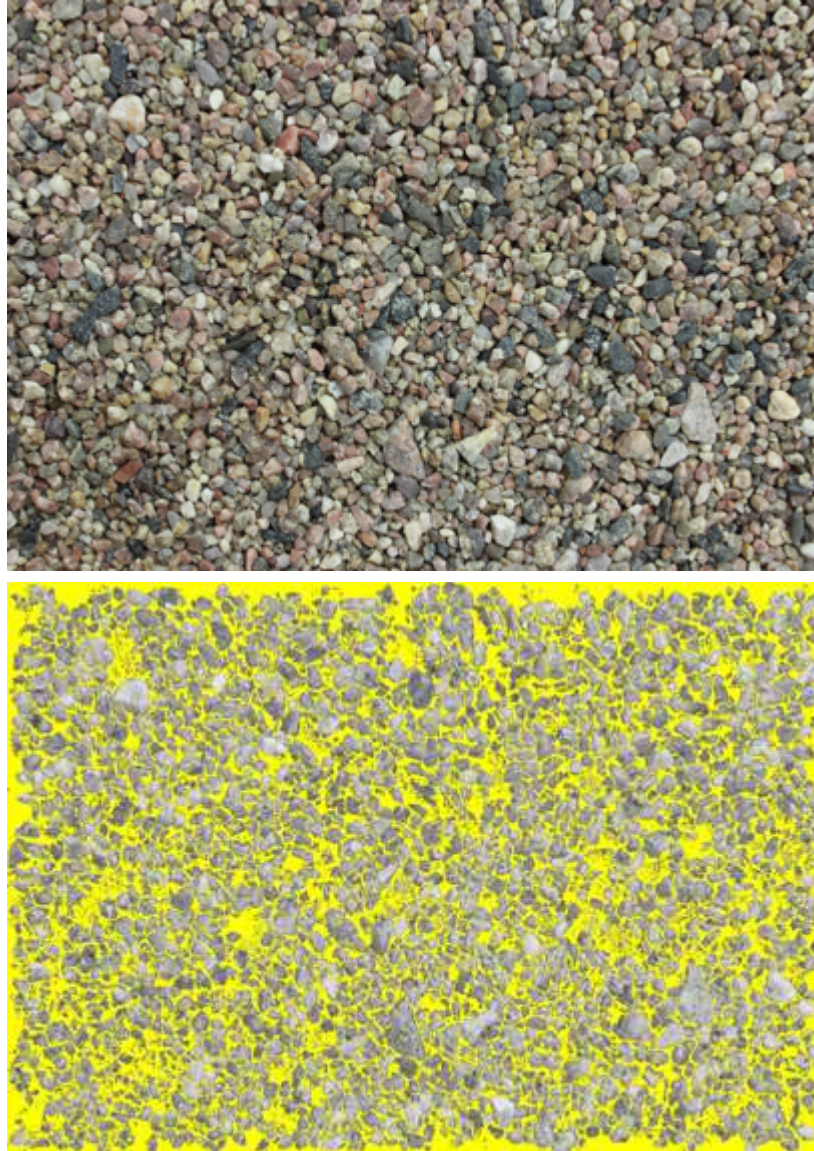
Figure 5. Original photograph (*top*) used for calibration and validation of the photo analysis parameters. Photo overlap (*bottom*) produced by the photo analysis process, using the "best fit" parameters.

2.3.4 Velocity and shear stress

In Runs 2 and 3, the velocity field was measured using a side-looking Nortek Vectrino+ acoustic Doppler velocimeter (ADV), which collects three-dimensional velocity measurements in a 6-mm diameter sampling volume at up to 200 Hz. Velocity measurements were performed

once equilibrium was reached in the channel. Cross-sections, located 0.3 to 1 m apart (with

closer spacing through the pools) were specified and at each cross section the ADV was used to

collect velocity profiles at 10-cm spacing across the channel. The vertical spacing of

measurements within each velocity profile was 2 cm, and velocity was measured at each

individual point for 1 minute. The resulting velocity data were time-averaged for each collection

location and filtered based on reported error (standard error rates greater than 0.003 m/s were

removed). Bed and water surface elevations were recorded at each velocity profile location. The

error associated with the elevation measurements was estimated as 1 cm.

The near-bed velocity measurements were used to compute local boundary shear stress

using the so-called single velocity method, described in Dietrich and Whiting (1989) and used

successfully in Nelson et al.'s (2010) gravel-bed flume study. The single velocity method is

derived from the law of the wall:

$$u(z) = \frac{u_*}{\kappa} \ln\left(\frac{z}{z_0}\right)$$

where $u(z)$ is the velocity at height z above the bed, z_0 is the roughness height, κ is von

Karman's constant ($\kappa = 0.4$), and u_* is the shear velocity, which is given as:

$$u_* = \sqrt{\frac{\tau}{\rho}}$$

where τ is the boundary shear stress and ρ is the density of water. These two relationships can be

condensed to:

$$\tau = \rho \left[\frac{u(z)\kappa}{\ln\left(\frac{z}{z_0}\right)}\right]^2$$

The roughness height (z_0) can be estimated as:

$$z_0 = 0.1D_{84}$$

where D_{84} is the grain size in which 84% of the bed surface grains are finer (Leopold and Wolman, 1957). The grain size values used were those obtained from the automated analysis of the bed photographs. The velocity and respective heights (z) used were those measured closest to the bed. The calculation error is related to both the velocity and elevation (or height) measurement error which were <0.003 m/s and 1 cm respectively.

2.3.5 Sediment transport rates

Bedload exiting the flume was collected in the downstream sediment trap. When the trap became full, it was shoveled out and the sediment was dried, weighed, and sieved to determine the average bedload transport rate at the outlet.

During the curved channel experiment (Run 3), bedload transport measurements within the channel were collected over cross sections spaced 0.3 to 1 m apart in the downstream direction. The cross-sections were closer to each other through the pools and many overlapped with the cross-sections where velocity measurements were taken. Bedload was collected at 20 cm increments across each cross section, resulting in 6 measurements at each section. Bedload samples were captured with a mini Helley-Smith device with an opening size of 7.6 x 7.6 cm over the course of two minutes. Each sample was dried and sieved to yield a transport rate and grain size distribution of transported sediment at each point.

The bedload samples represent the downstream component of the sediment transport vector. Following Dietrich and Smith (1984) and Nelson et al. (2010), I can use these measurements to calculate cross-stream bedload transport rates by taking advantage of the fact that the bed was at steady state conditions.

The sediment continuity equation in a streamwise curvilinear coordinate system is

$$\frac{1}{1-N}\frac{\partial q_s}{\partial s} - \frac{q_n}{(1-N)R} + \frac{\partial q_n}{\partial n} = -(1-p)\frac{\partial \eta}{\partial t}$$

where s is the streamwise-oriented downstream coordinate, n is the cross-stream coordinate orthogonal to s, q_s is the downstream component of the volumetric sediment transport rate per unit width, q_n is the cross-stream component of the volumetric sediment transport rate per unit width, R is the radius of curvature of the channel centerline, p is the bed porosity, η is the bed elevation, t is time, and $N = n/R$. Under steady state, $\partial \eta / \partial t = 0$, and the resulting equation can be discretized and solved for q_n, resulting in the following expression for q_n at node (i,j):

$$q_n(i,j) = \frac{\left[-\frac{1}{1-N}\frac{q_s(i,j)-q_s(i-1,j)}{\Delta s} + \frac{q_n(i,j-1)}{2(1-N)R(i,j)} + \frac{q_n(i,j-1)}{\Delta n} \right]}{\left[\frac{1}{\Delta n} - \frac{1}{2(1-N)R(i,j)} \right]}$$

where Δs is the distance along the centerline between bedload cross sections and Δn is the cross-stream spacing between measurements. The local radius of curvature, $R(i,j)$, is calculated as

$$R(i,j) = \frac{(x'^2 + y'^2)^{3/2}}{x'y'' - y'x''}$$

where

$$x' = \frac{\partial x}{\partial s}, \qquad x'' = \frac{\partial^2 x}{\partial s^2}, \qquad y' = \frac{\partial y}{\partial s}, \qquad y'' = \frac{\partial^2 y}{\partial s^2}$$

where x and y are the local channel centerline coordinates.

This calculation for q_n is performed by starting at one of the flume walls and setting q_n there equal to zero, then working across the channel.

3. RESULTS

The following section details the results from the three experimental runs. Table 4 summarizes the hydraulic and geomorphic conditions observed during each flume run.

Table 4. Sediment/Flow Parameters

	Run 1	*Run 2*	*Run 3*
Run Duration (hrs)	75	26	45
Channel Width (m)	1.35	1.35	1.35
Length (m)	12.19	12.19	12.57
Initial Slope (m/m)	0.0068	0.0047	0.0066
Final (Equilibrium) Slope (m/m)	0.0052	0.0037	0.0057
Average Depth (m)	0.05	0.055	0.066
Water Discharge (cms)	0.035	0.033	0.038
Average Velocity (m/s)[1]	0.519	0.444	0.426
Mean Shear Stress (Pa)[4]	2.37	1.85	3.36
Boundary Shear Stress (Pa)[3]	-	2.12	1.37
Sediment Feed Rate (kg/hr)	59	59	59
Average D_{50} (of bed) (mm)	-	4.98	7.22
D_{50} of Supply (mm)	4	4	4
Mean Shields Stress[2]	0.037	0.029	0.052

1) Average Velocity (v)

$$v = Q/A$$

Where Q is discharge (cms) and A is average cross-sectional area (m^2).

2) Shields Stress (τ_*)

$$\tau_* = \frac{\tau}{(\rho_s - \rho)gD_{50}}$$

Where τ is mean shear stress (Pa), ρ_s is the sediment density (kg/m^3), ρ is the density of water (kg/m^3), g is the gravitational constant (9.81 m/s^2), and D_{50} is the grain size in which 50% of the bed surface grains are finer.

3) Average Boundary Shear calculated using the single velocity method (see Methods)

4) Average Shear Stress

$$\tau = \rho g R_h S$$

Where ρ is the density of the fluid (water) (1000 kg/m³), g is the gravitational constant (9.81 m/s²), S is the channel slope, and R_h is the average hydraulic radius of the channel (m).

3.1. Run 1: Straight channel, no obstruction

The first run in the straight channel lasted for 75 hours. During Run 1, a total of 12 Structure-from-Motion (SfM) datasets were collected. Figure 6 illustrates the resulting digital elevation models. These elevation models display the bed evolution over the 75 hour run time. The bed topography during Run 1 was very dynamic. Althoughthere are fairly persistent bed features, such as the bars located at the upstream and downstream ends, most of the features were ephemeral and bar movement was very episodic.
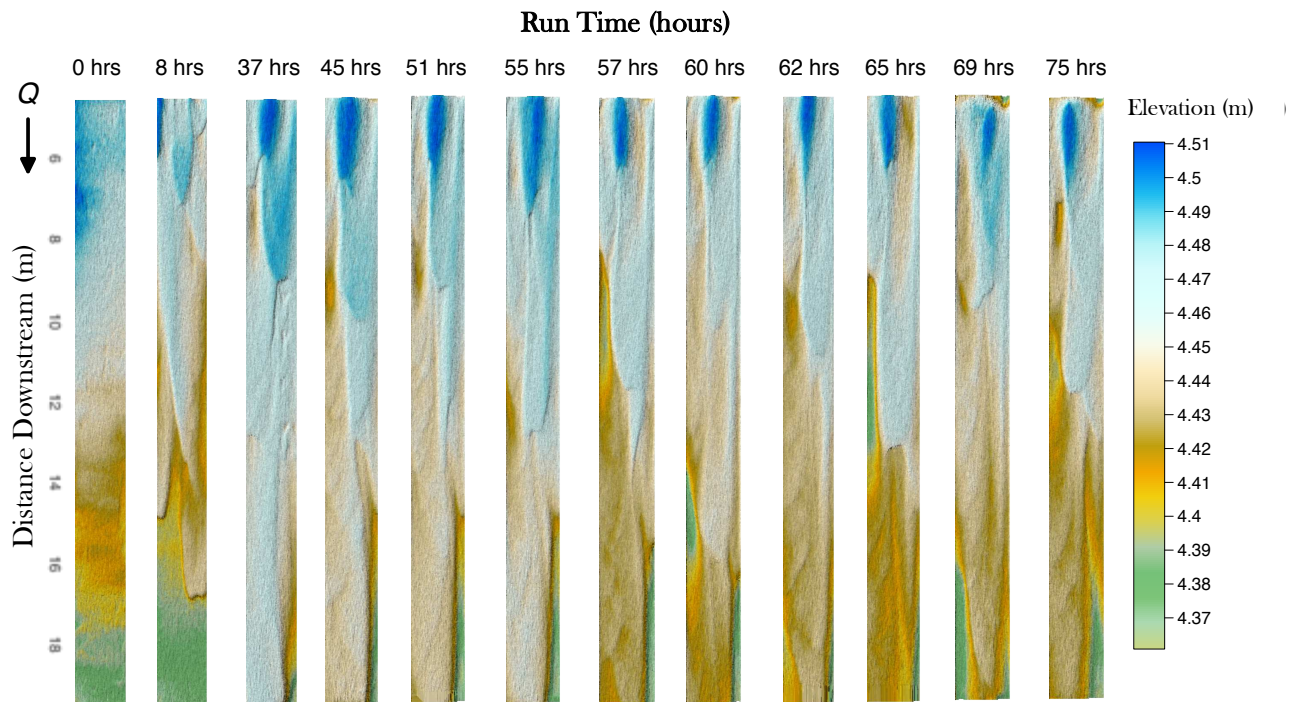

Figure 6. Series of elevation models that illustrate the bed activity over the 75-hour run time.

Figure 7 presents detrended bed elevation data from Run 1, where the mean slope was subtracted from each digital elevation model. This emphasizes the local bar-pool topography, and the channel is clearly dynamic without ever stabilizing on a static bed configuration.
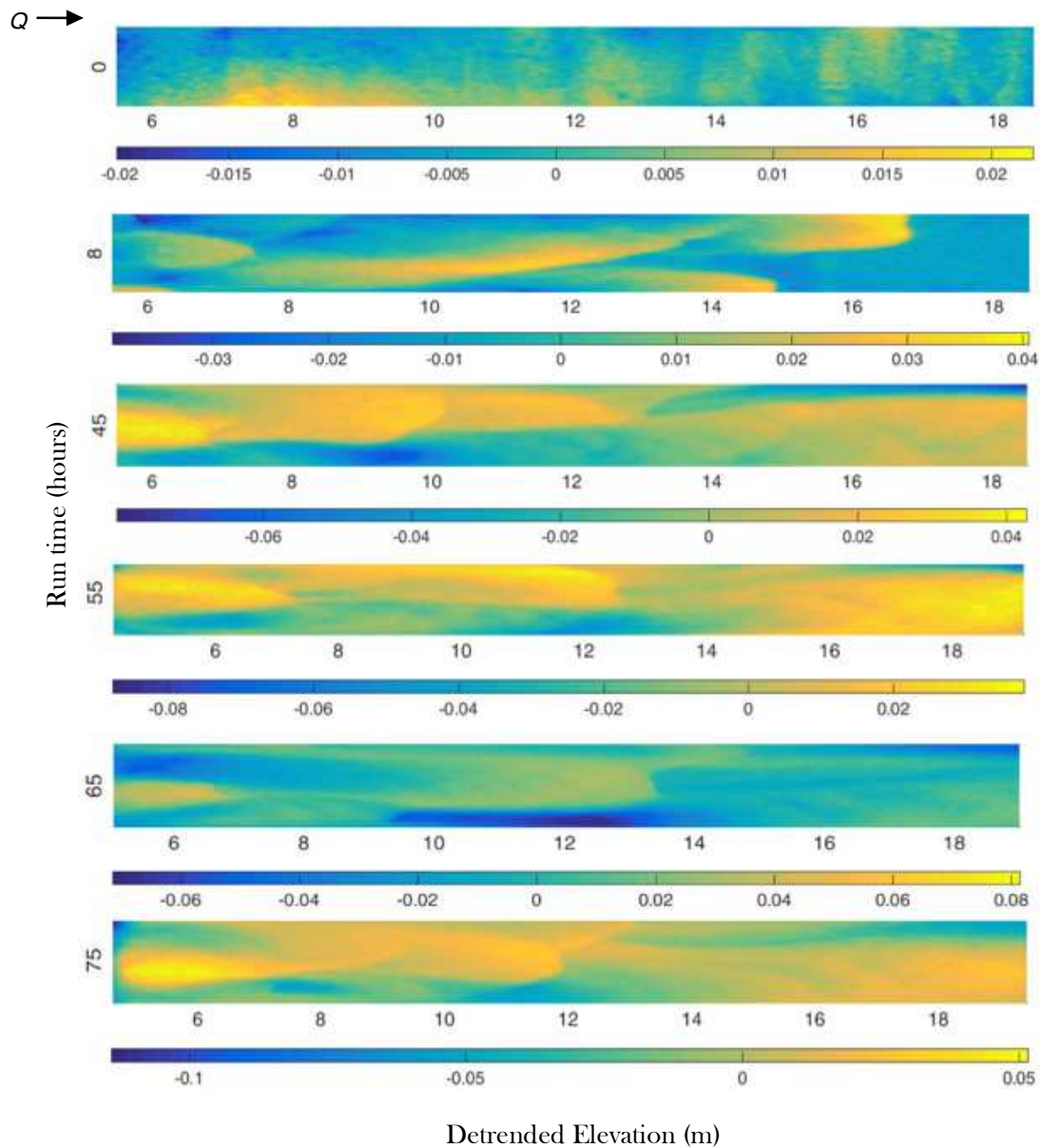

Detrended Elevation (m)

Figure 7. Digital elevation models featuring detrended elevations given for each of the time steps during the duration of the model run. Detrended elevations (rather than absolute elevations) better depict relative pool and bars sizes.

One of the indicators that was used to determine channel equilibrium was the comparison between the incoming and exiting sediment flux. This did not stabilize until the very end of the run time, which makes sense due to the pulse-like nature of the free bars. Figure 8 gives the sediment measured in the trap over the simulation period.
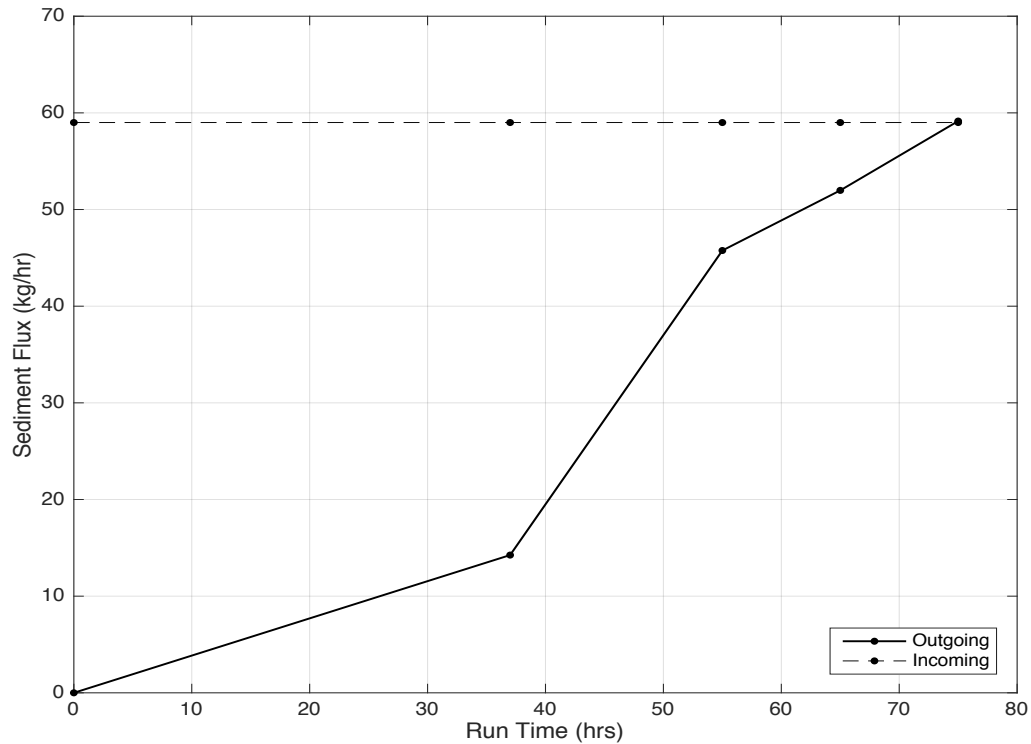

Figure 8. Comparison of the expected sediment supply (based on the sediment feed rate) and the actual outgoing sediment load. Convergence of the two is shown after 65 hours.

The other indicator of channel equilibrium was the bed slope. The evolution of the slope over the course of the 75 hours can be seen in Figure 9 below. The channel adjusted itself by aggrading quite a bit in the initial 30 hours throughout the entire length of the channel. The initial slope was around 0.007, but from 45 to 75 hours, the slope stabilized at around a value of 0.005.
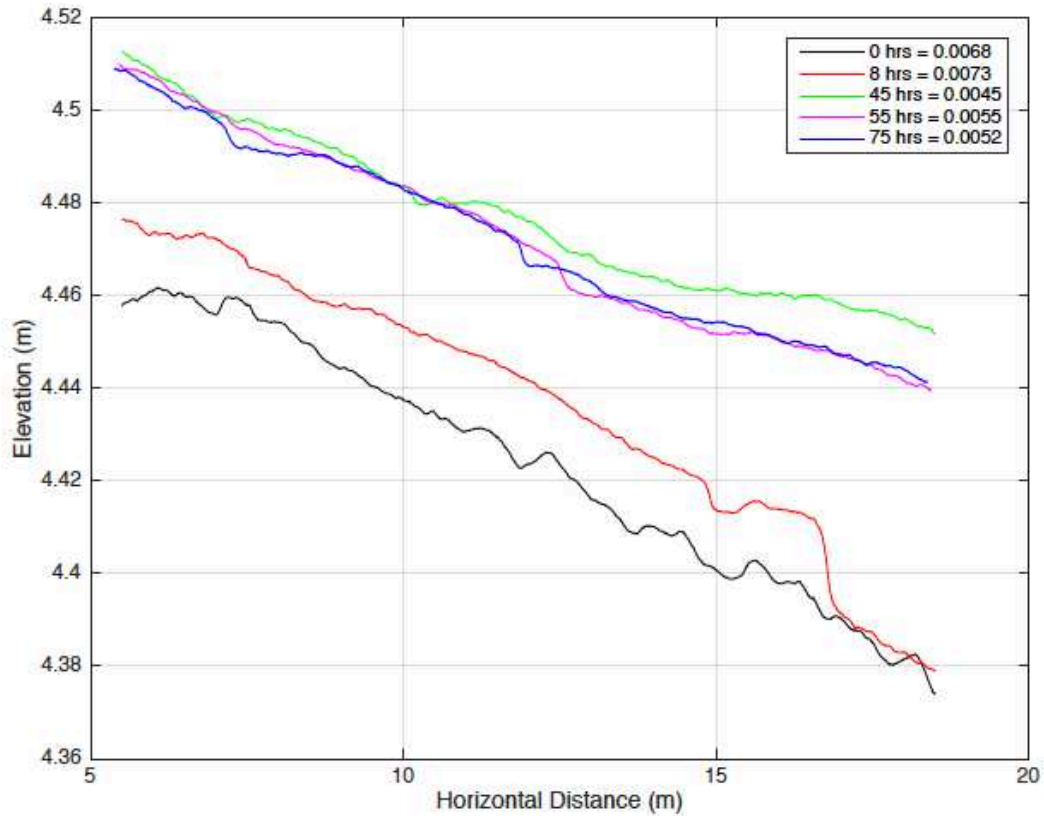
Figure 9. Change in the longitudinal profile over the 75-hour run time. The channel aggraded significantly between 8 hours and 45 hours, in addition to decreasing its overall slope. Mean bed slope at each time is provided in the figure legend.

Over the simulation period, stable alternate bars (or forced bars) never developed, but migratory topographic lobes were observed. These lobes behaved like free bars, migrating quite rapidly though the channel. Their migration was mapped using the SfM datasets and records of the bar front locations that were collected periodically by visual inspection while the experiment was taking place. These lobes were very dynamic in nature and sometimes difficult to track due to their tendency to consolidate into unified sediment fronts. The figures given below display their migration patterns throughout the channel (Figure 10), in addition to their migration rates (Figure 11) which were surprisingly steady, especially towards the end of the run time.
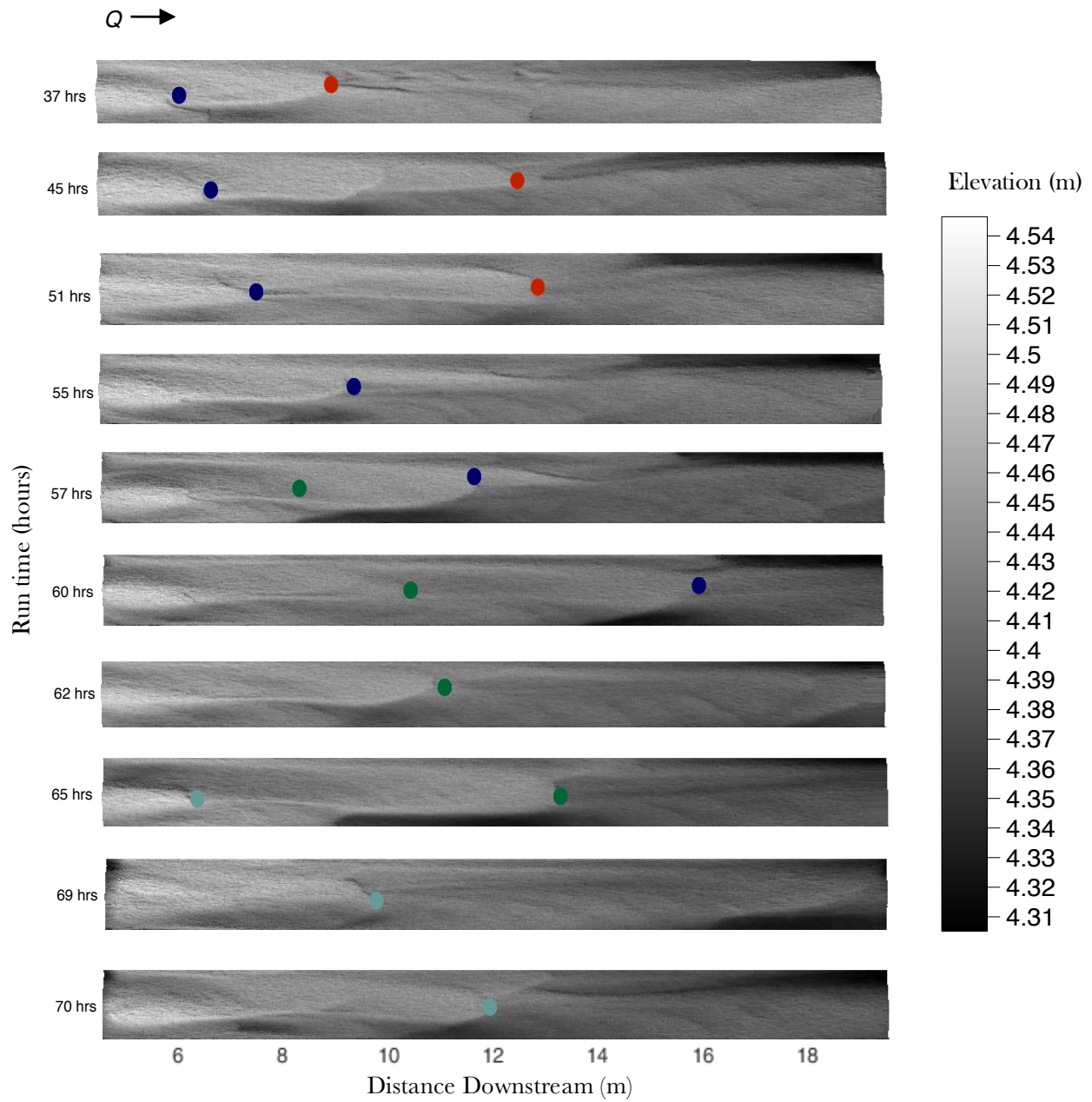
Figure 10. Tracking lobe migration while the bed evolved in a very dynamic manner. Some bars were easy to track, while others quickly merged or disappeared.
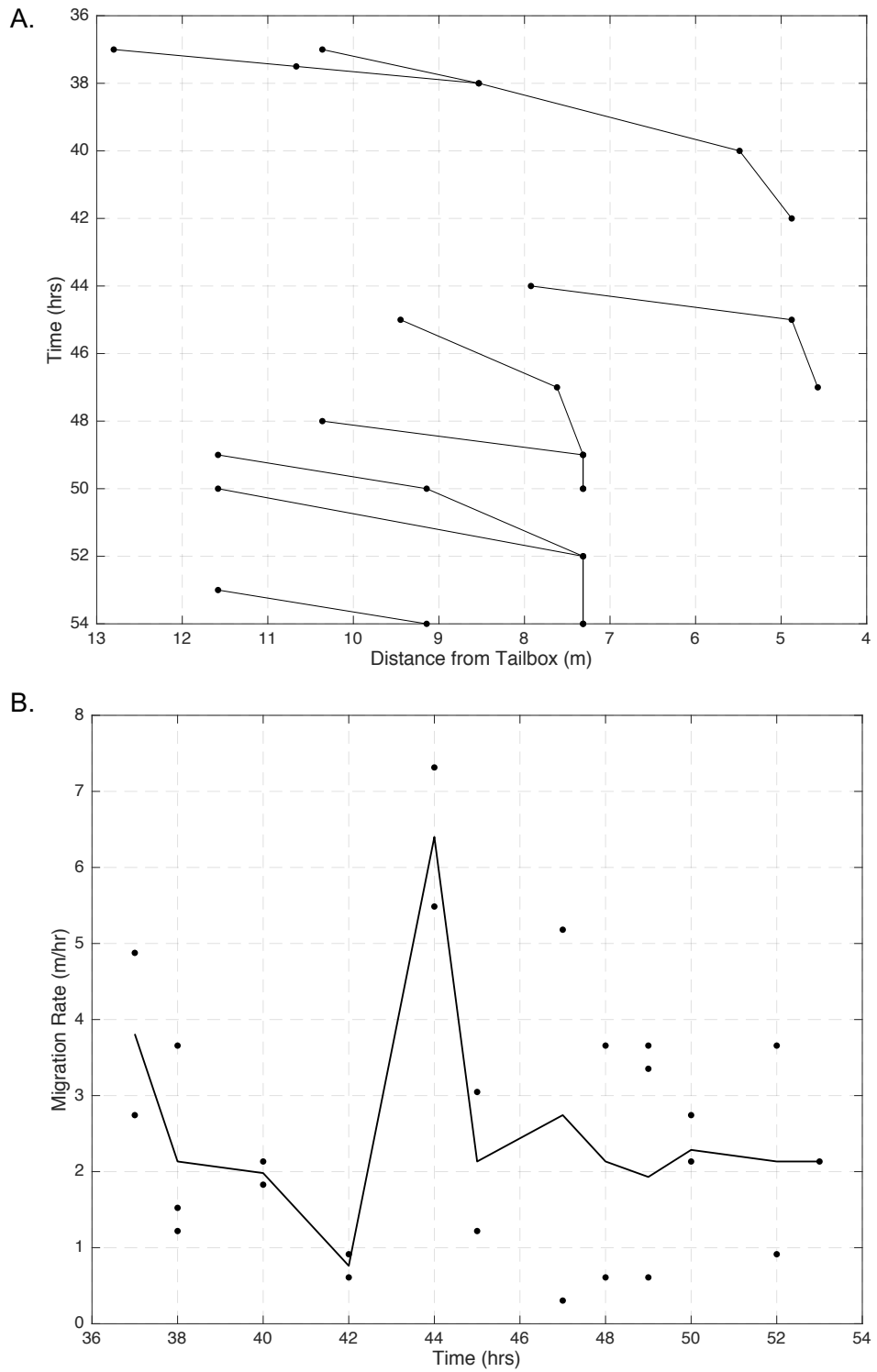
Figure 11. Migration paths were recorded for bar fronts as they moved downstream (Figure 11A.). Bar front locations yielded migration rates for each of the discrete free bars that were observed (Figure 11B.).

3.2. Run 2: Straight channel, with an upstream obstruction

Run 2 involved the introduction of an upstream obstruction to induce a "forced" pool and bar formation. Compared to Run 1, equilibrium was reached much faster in this channel, after 26 hours. Convergence of the incoming and outgoing sediment loads can be observed in Figure 12. Six Structure-from-Motion datasets were collected during the duration of the flume run (in 5 hour increments). The graph given below in Figure 13 shows the slope evolution, which is fairly insignificant when compared to the change that occurred in the first run. No excessive rates of aggradation or degradation were observed. Free bars were observed migrating over the top of the forced bar and through the forced pool at the beginning of the simulation; however, this was short-lived. It did not take long for the bed topography to became stable in the channel.
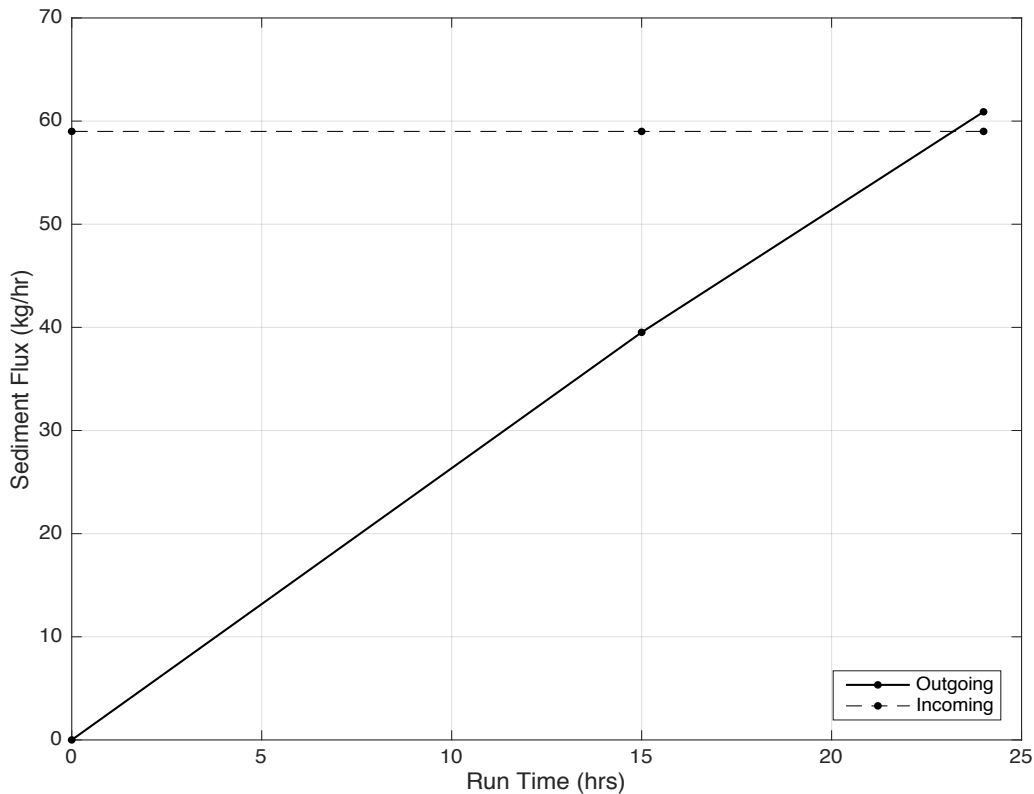
Figure 12. Comparison of the sediment feed (expected outgoing sediment) and the observed outgoing sediment load. Convergence of the two was observed around 24 hours.

Figure 13. Evolution of the channel's longitudinal profile during run 2 in the straight channel configuration. Mean bed slopes are provided in the figure legend.

Figure 14 (below) shows digital elevation models (DEMs) that were produced from the Structure from Motion datasets. These DEMs display the growth of the point bar and pool at the upstream end of the channel.
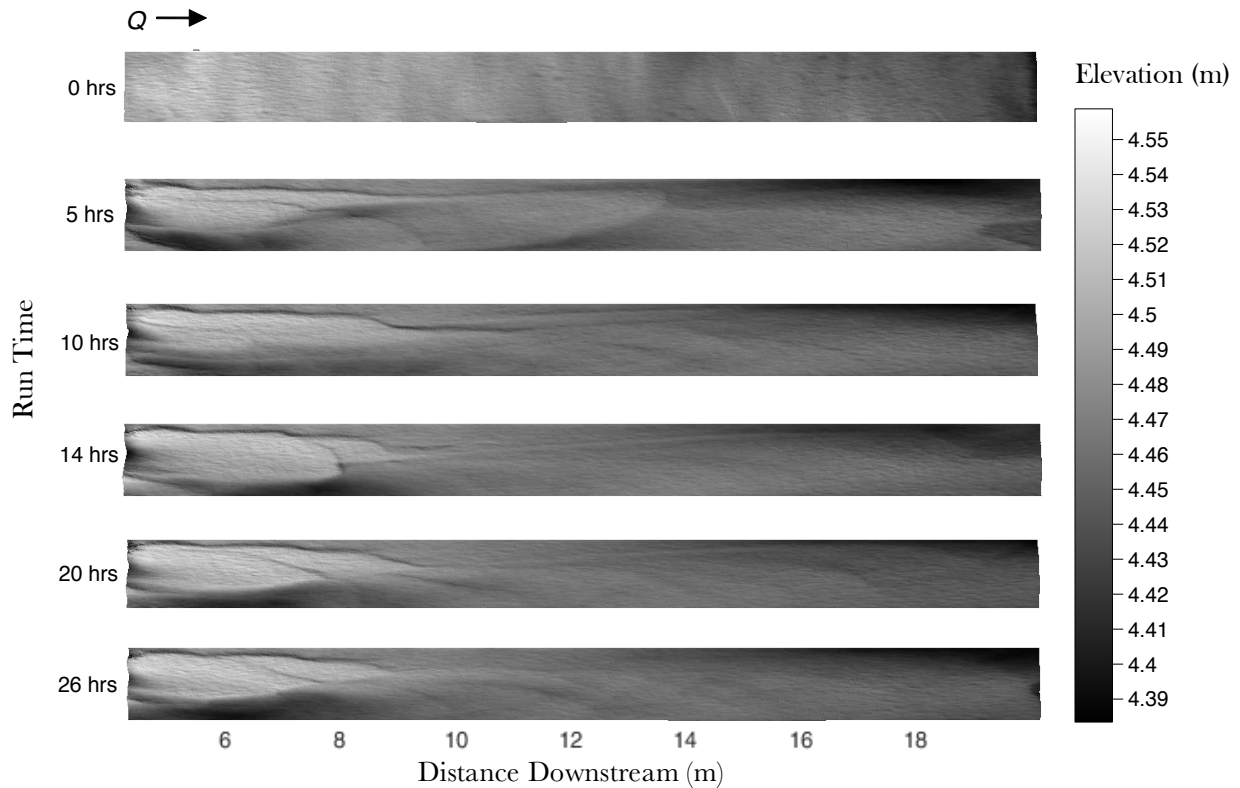
Figure 14. Evolution of the straight channel under the influence of hydraulics induced by the upstream obstruction.

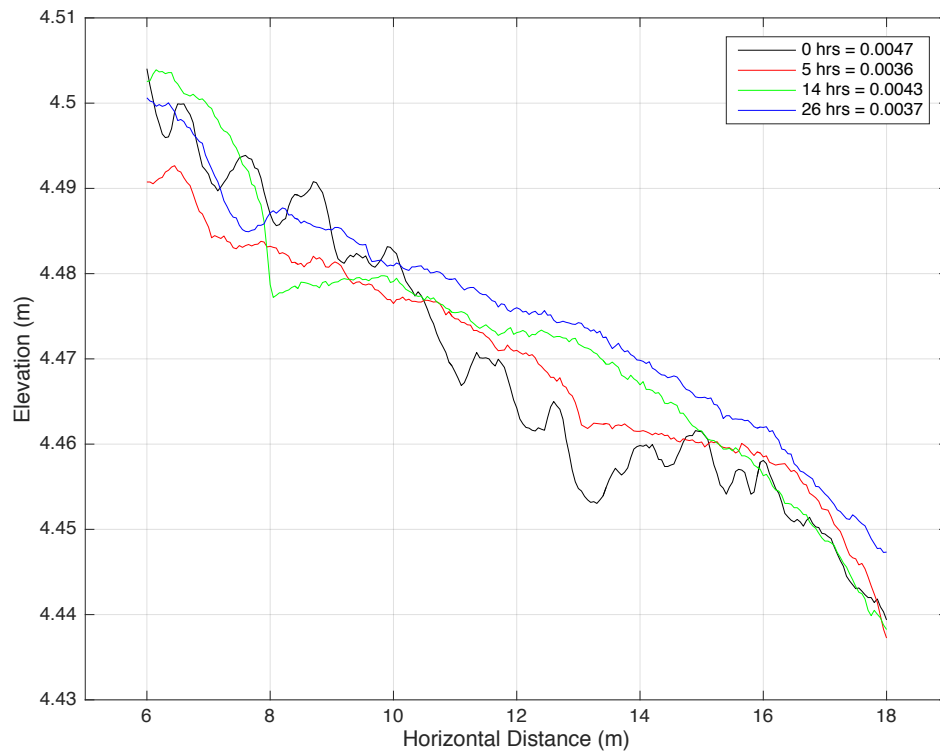The following graphic (Figure 15) displays the detrended elevations (each DEM was subtracted from the mean channel slope to produce the elevation differences) given over the simulation period. The detrended elevation maps clearly show the growth of the upstream pool and bar over the 26 hours. While the pool became deeper, the bar height increased. Both features lengthened longitudinally.
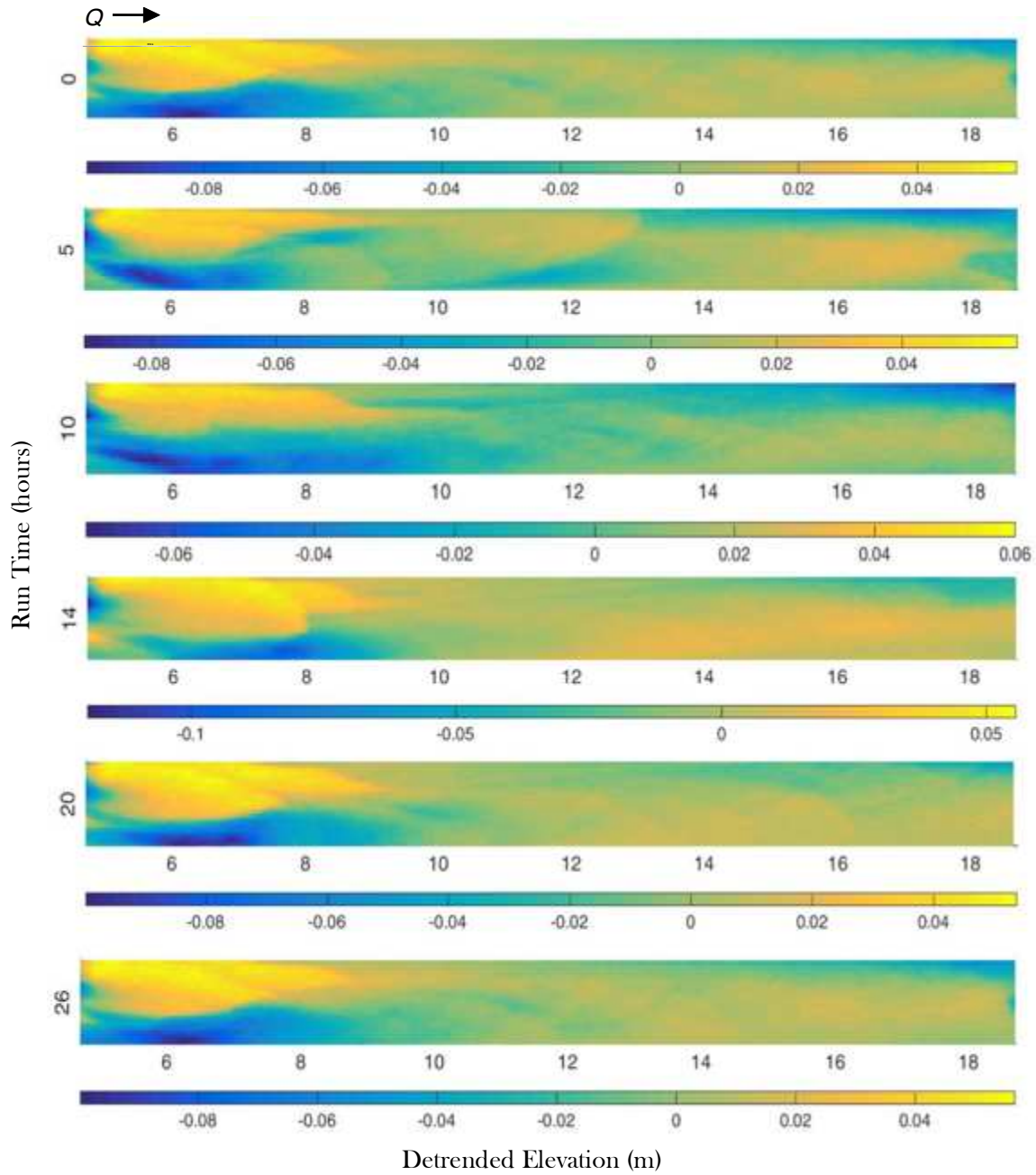
Figure 15. Detrended elevations given in ~5 hour increments for run 2 of the straight channel. These DEMs nicely display the growth of both the upstream pool and bar forced by the channel obstruction.

Figure 16 (given below) displays the cross-sections (within the upstream pool/bar region) in which velocity measurements were collected, along with the corresponding detrended elevations.
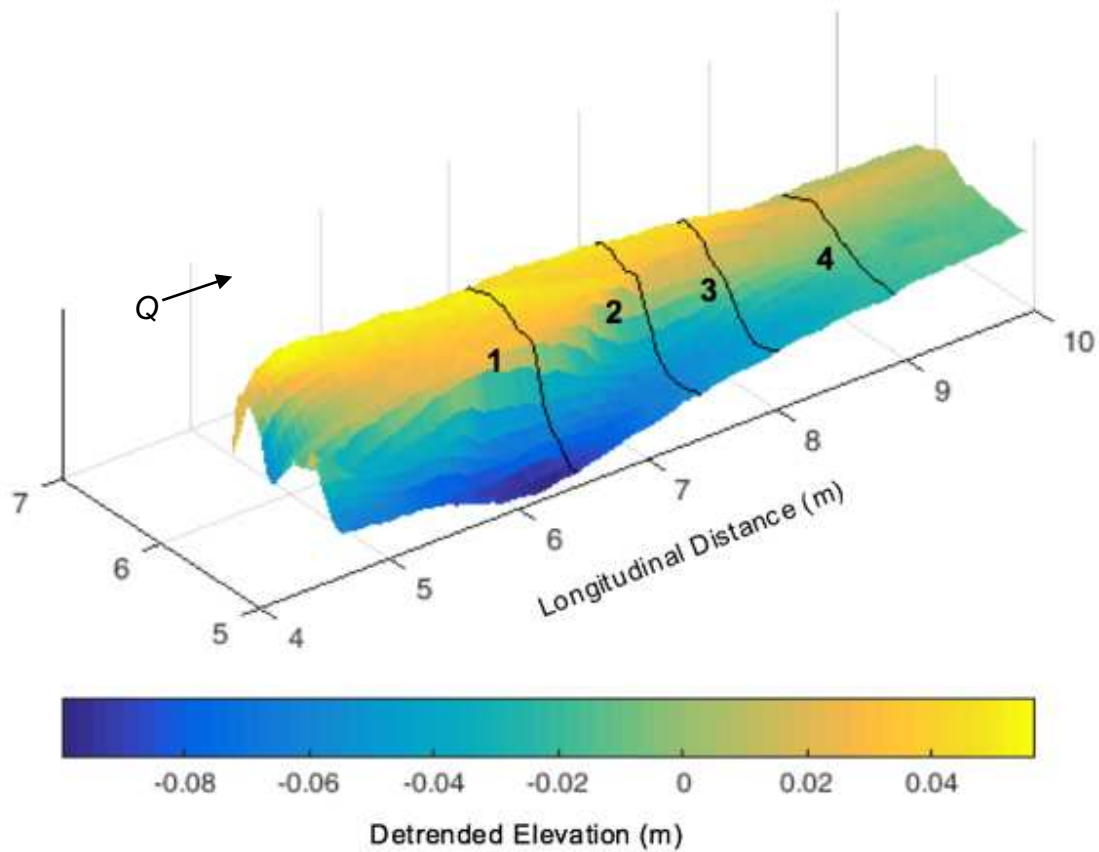
Figure 16. Positions of velocity cross-sections (1-4) through the upstream forced bar/pool feature.

The series of graphs (Figure 17) shown below feature the velocity measurements. Each point represents a location where a velocity measurement was collected and time-averaged. The velocity magnitudes (in m/s) are color-coded and are superimposed over the channel bed. The velocities represented are the downstream component of the total channel velocity at each measurement point.

31

A.

B.
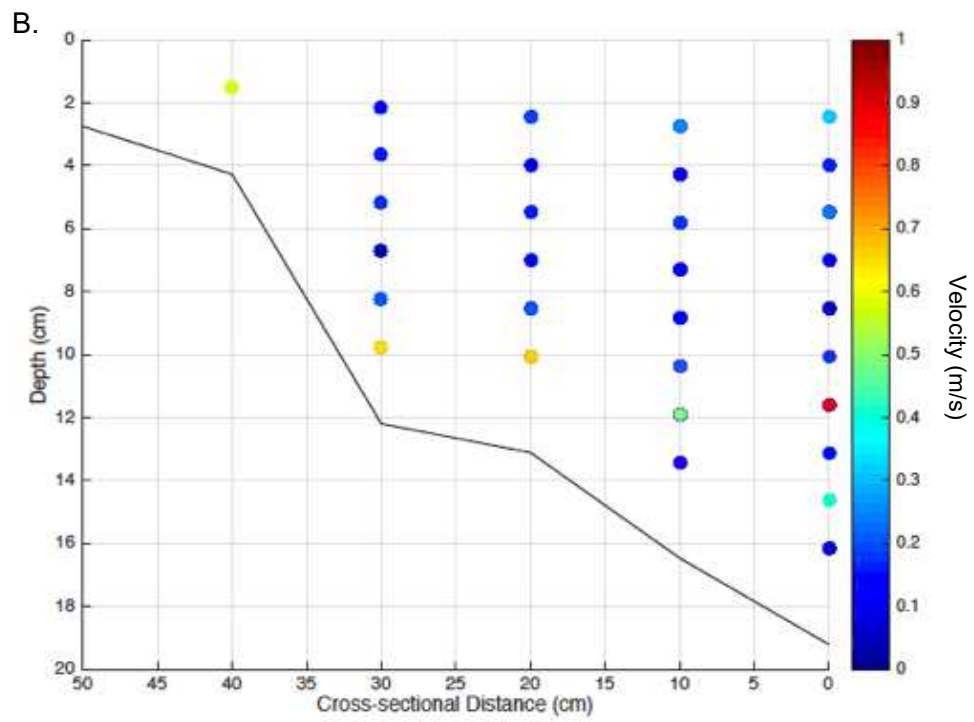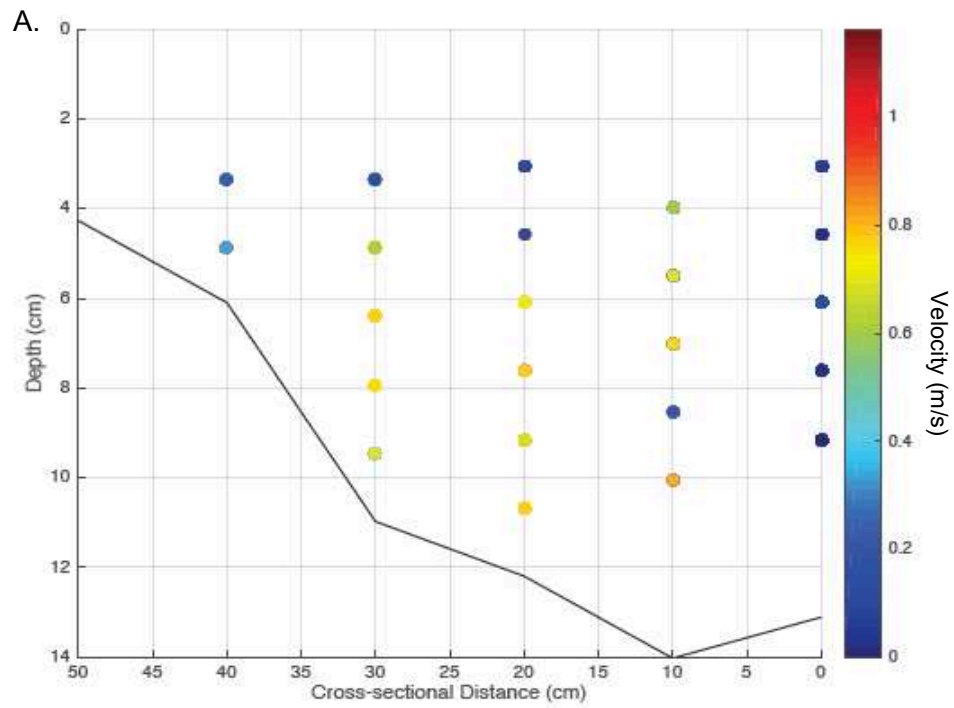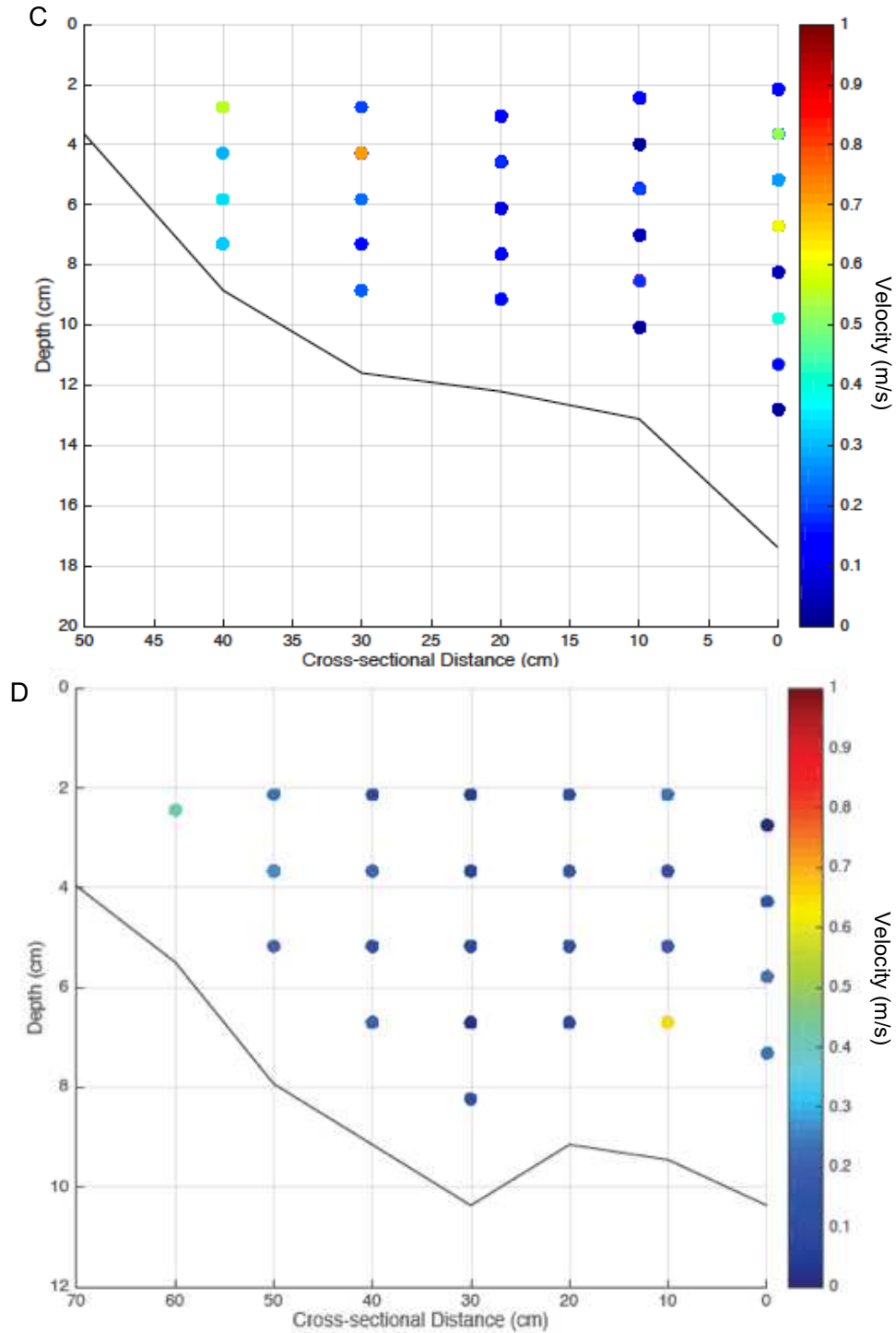
Figure 17. Velocities measured at each cross-section shown in *Figure 16*. Cross-section 1 (*Figure 17A*.) is located 1.82 meters from upstream end of channel and at the head of pool. Cross-section 2 (*Figure 17B*.) located 2.74 meters from upstream and in the middle of pool. Cross-section 3 (*Figure 17 C*.) is located 3.66 meters from upstream and in the middle of the pool. Last, cross-section 4 (*Figure 17D*.) is located 4.27 meters from upstream and at the end of the pool.

In addition to time-averaging the velocities at each point of measurement, the velocities were

averaged spatially (within the water column). Figure 18 gives the velocity profiles obtained for

each cross-section after averaging the velocity in time and space.
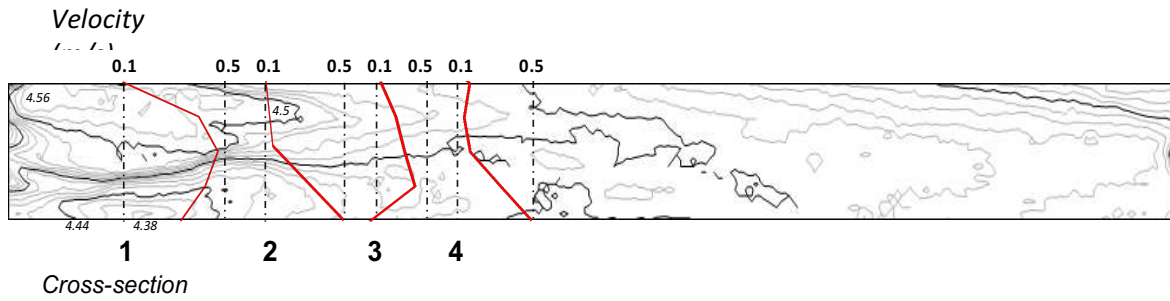
Figure 18. Average velocity profiles for each cross-section layered over bed topography contours (showing the high and low points of interest). Flow direction is from left to right. Elevations (in meters) of key contours are given in italics.

Figure 19 shows the boundary shear stress profiles calculated using the single-velocity method, at each of the velocity cross-sections.
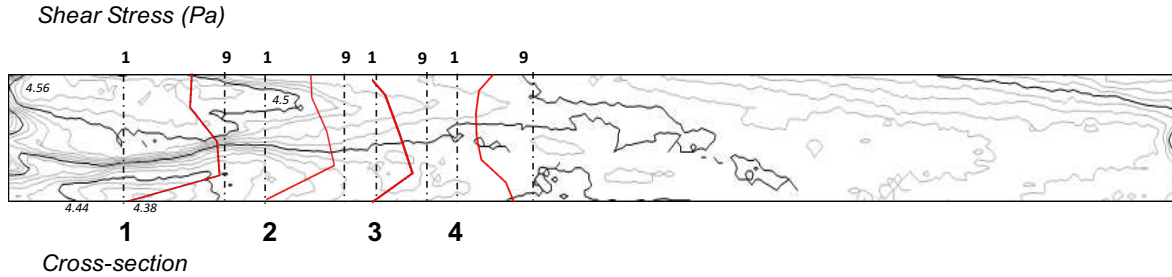
Figure 19. Boundary shear stress profiles for each cross-section layered over bed topography contours (showing the high and low points of interest). Flow direction is from left to right. Elevations (in meters) of key contours are given

The average geometric standard deviation (σ_g) of the bed at the end of Run 2 was 1.60. A map of the median bed surface grain sizes estimated from each photograph of the bed are presented in Figure 20. In general, there was not a strong sorting pattern established during this run.
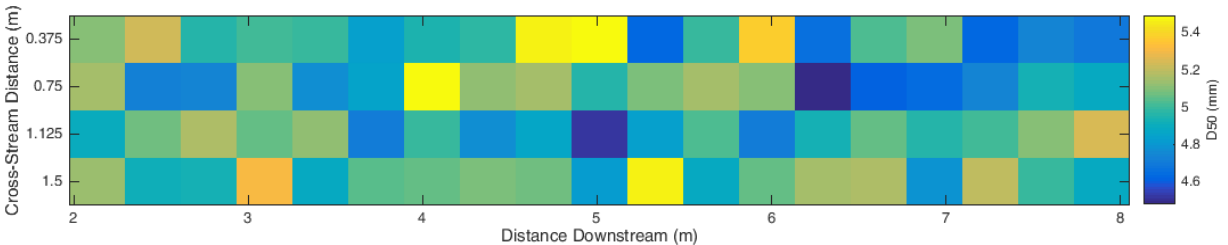
Figure 20. D50 grain size bed surface values for the straight channel with an upstream barrier (run 2).

3.3. Run 3: Curved channel

Run 3 had a duration of 45 hours, at which point the sediment transport rate exiting the

flume approximately matched the sediment feed rate (Figure 21).
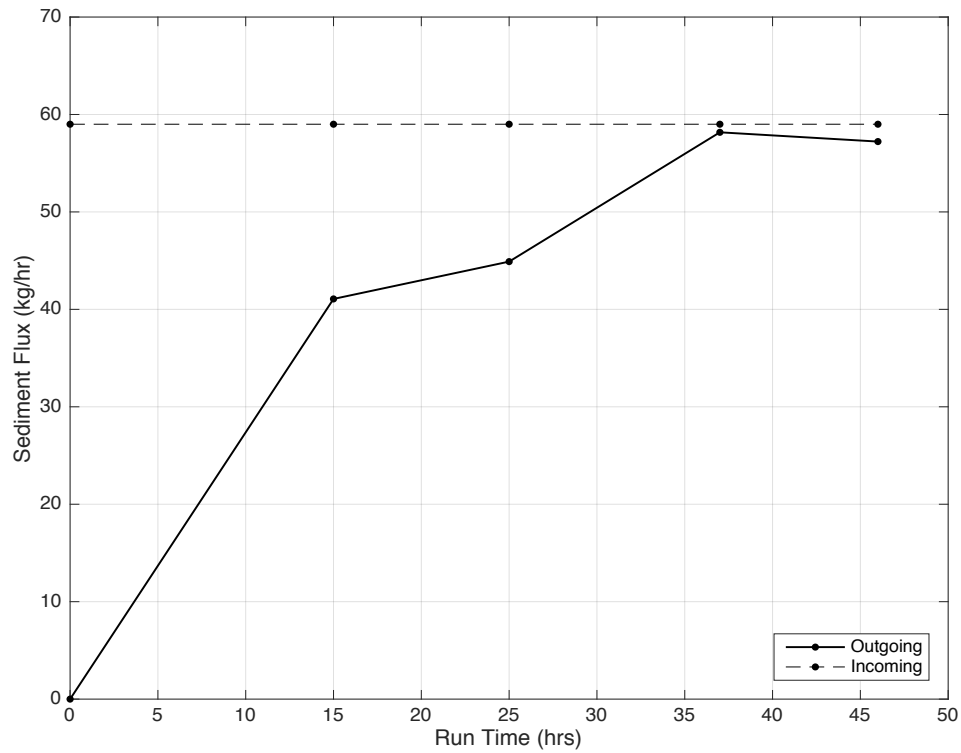
Figure 21. Comparison of the sediment feed (expected outgoing sediment)
and the observed outgoing sediment load. Convergence of the two was
observed around 37 hours.

During the simulation duration, a total of six SfM datasets were collected. The resulting

digital elevation models (DEMs) are given in Figure 22 (below).
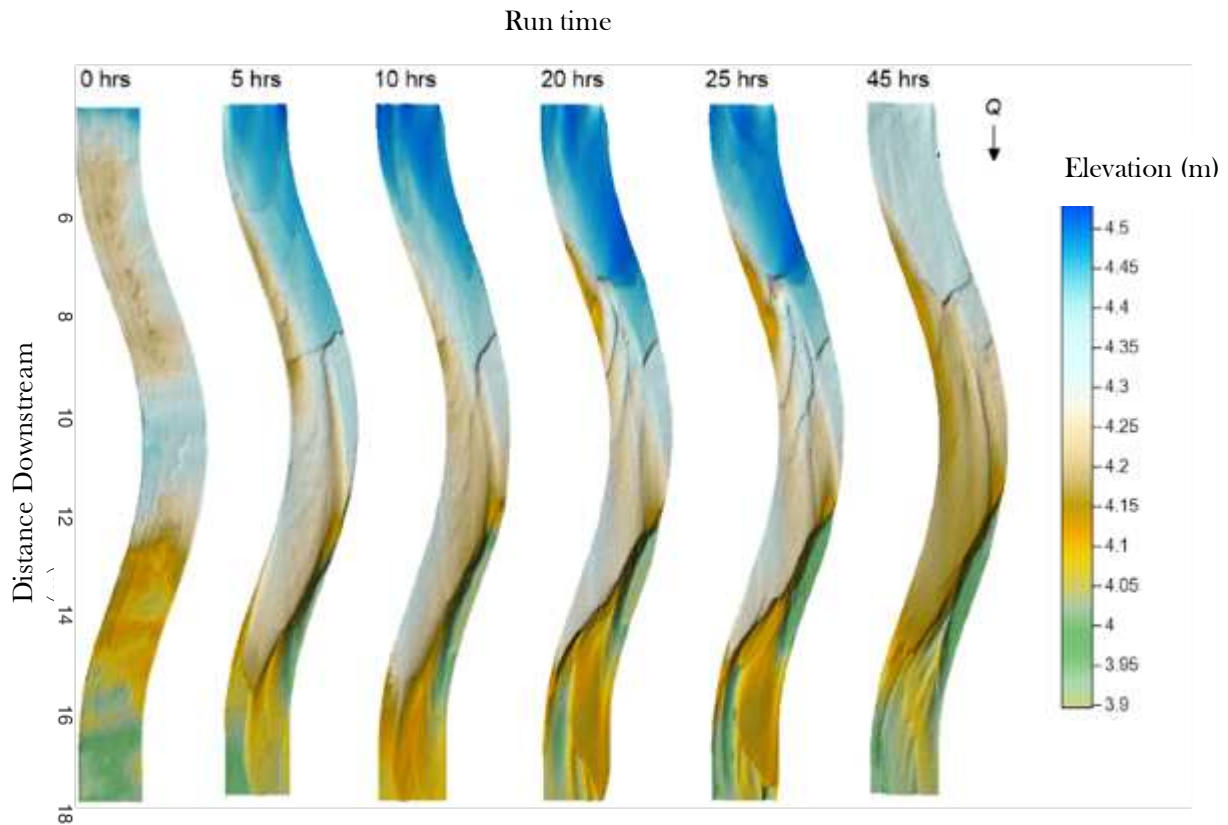
Figure 22. Evolution of the curved channel over the course of 45 hours. The DEMs show the growth of two major pools (one upstream of the inside of the meander and one downstream of the outside of the meander).

Free bars were observed moving through the channel on top of the forced bars (lobe migration can be seen in Figure 22). Migration of these bars seemed to slow significantly and finally halt once the channel was close to equilibrium. Once dynamic equilibrium was reached in the channel (determined based on incoming and outgoing sediment flux, channel slope, and movement of the bars within the channel), both velocity and bedload transport measurements were conducted and bed surface photos were collected. Figure 23 shows the cross-sections that

bedload transport and velocity were measured. The highest density of cross-sections was through

the upstream and downstream pools.
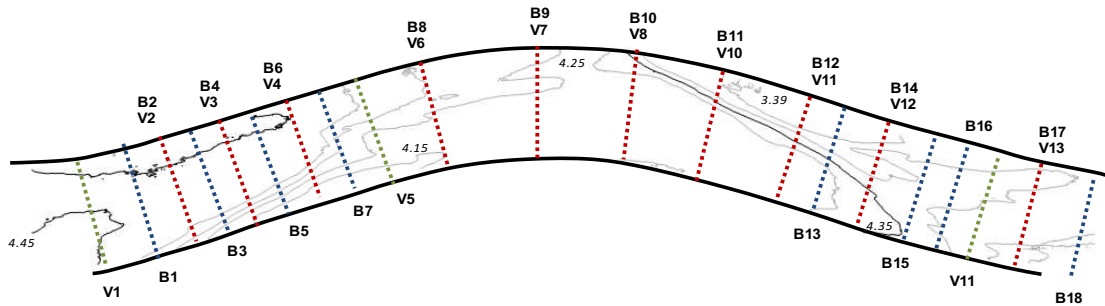
Figure 23. Bedload transport (B) and velocity (V) measurement cross-sections layered over bed topography contours. Flow direction is from left to right. Elevations (in meters) of key contours are given in italics.

After the channel was dewatered for the final time, bed surface photographs were taken. The automated image processing procedure described in the Methods section of the report was utilized to extract surface grain sizes from the digital photographs. The average geometric standard deviation (σ_g) of the meandering channel bed was 1.71. A map of the D50 grain sizes achieved for each section of the bed (defined by an individual photograph) can be seen in Figure 24 below.
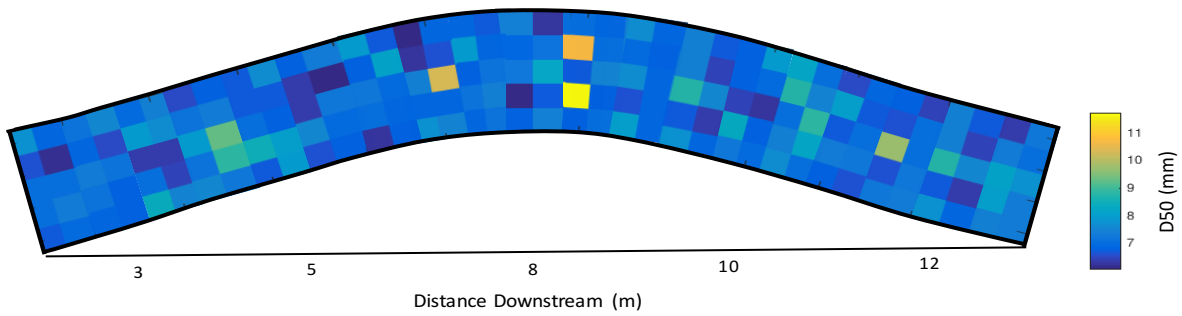
Figure 24. D50 grain size bed surface values for the straight channel with an upstream barrier (run 2).

Figure 25 presents velocity measurements in select cross-sections. Each point represents a location where a velocity measurement was collected and time-averaged. The velocity magnitudes (in m/s) are color-coded and superimposed over the channel bed. Zones showing the primary direction of secondary flow are also delineated, showing that in general the bend exhibited near-bed flow toward the inner bank and flow toward the outer bank at the water surface.
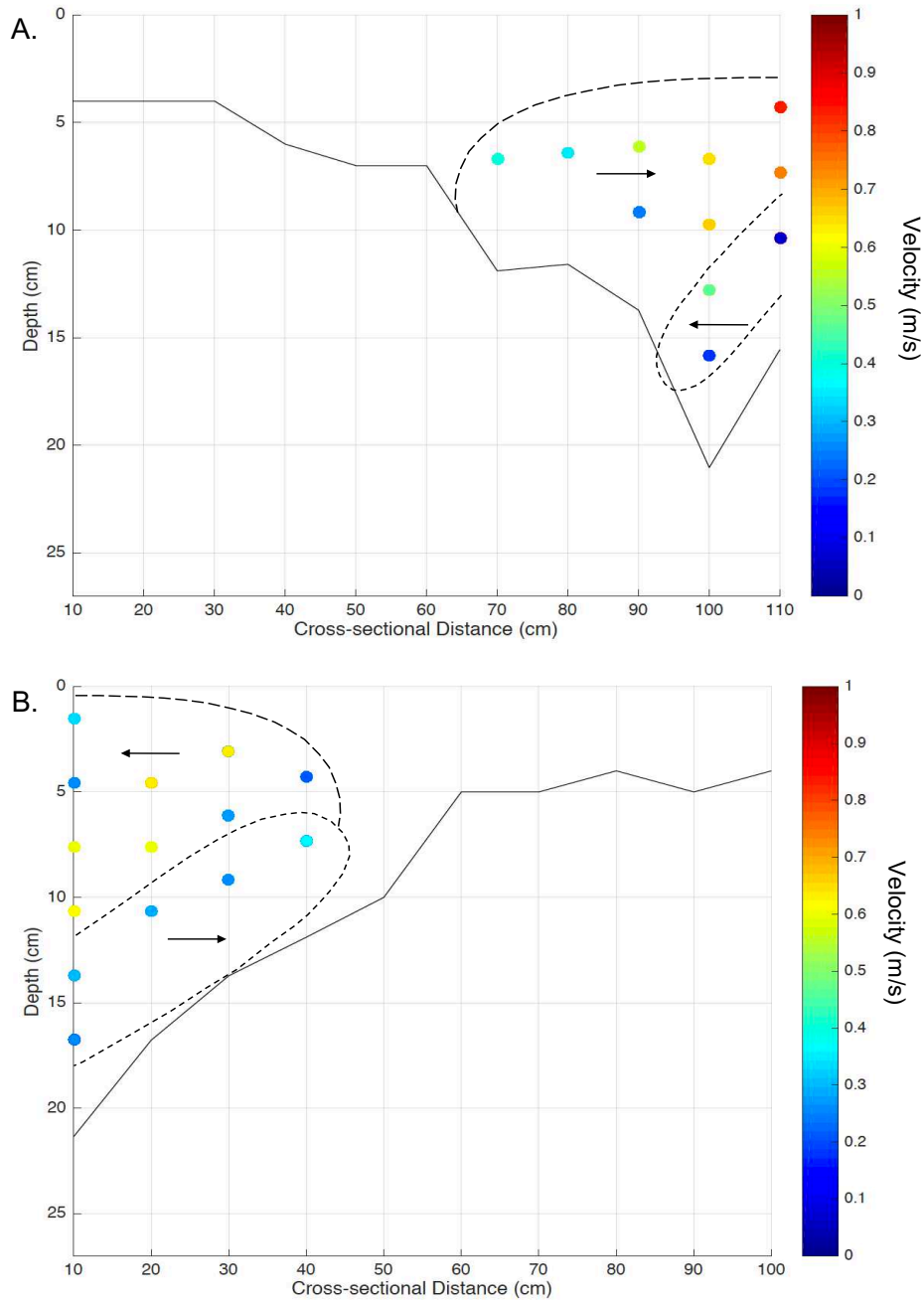
Figure 25. Velocities measured at select cross-sections shown in *Figure 23*. Cross-section *V1* (*Figure 25A*.) is located 5.18 meters from upstream end of channel and at the deepest point of the upstream pool. Cross-section *V13* (*Figure 25B*.) is located 11.3 meters from upstream and in the deepest point of the downstream pool. Cross-sectional distance is measured from the left "bank" of the channel. The velocity magnitudes indicated by the color ramp are the downstream component of the total channel velocity, while the arrows indicate the direction of the cross-stream component of the flow velocity.

In addition to time-averaging the velocities at each point of measurement, the velocities were averaged spatially (within the water column). Figure 26 gives the average downstream component of the velocity over each cross-section. These velocity profiles show that the high-velocity core shifts across the channel from the upstream pool, over the bar, and into the downstream pool.
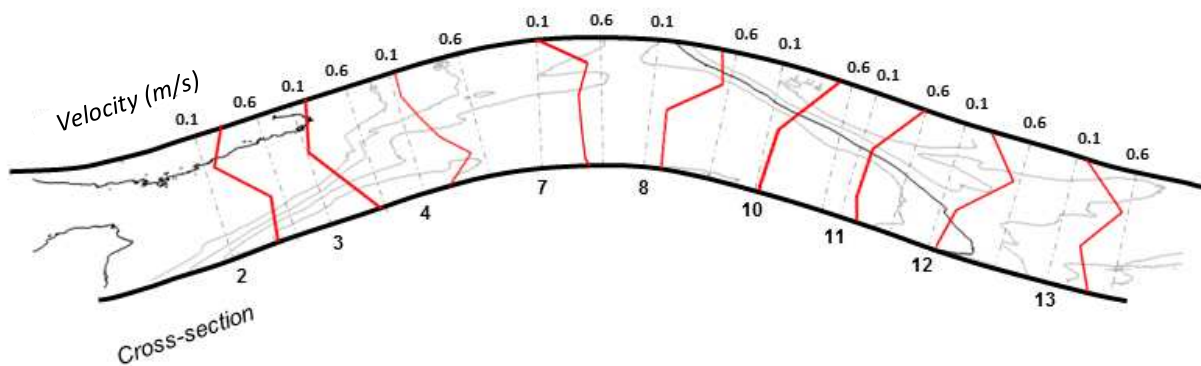
Figure 26. Average velocity profiles for each cross-section layered over bed topography contours (showing the high and low points of interest. Flow direction is from left to right.

Figure 27 presents boundary shear stress profiles computed from the single velocity measurements. In general, the shear stress showed patterns similar to the velocity, where the highest values occurred in the pools.
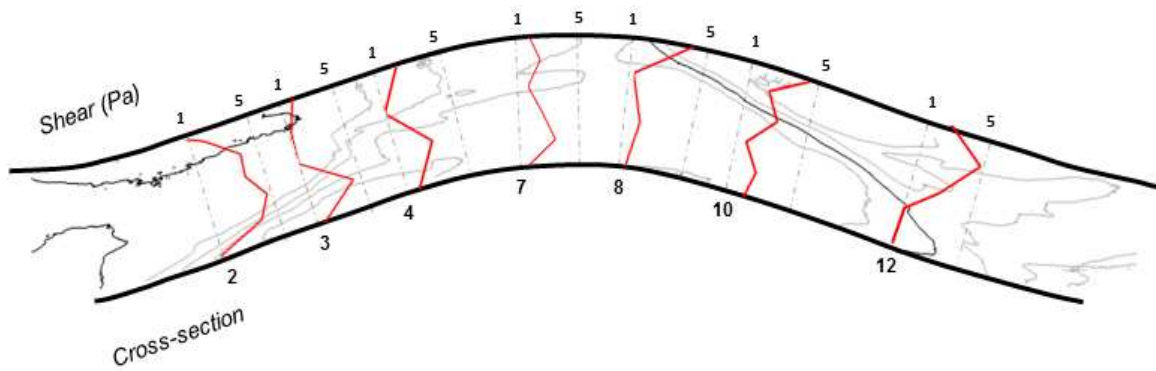
Figure 27. Boundary shear stress profiles for each cross-section layered over bed topography contours (showing the high and low points of interest). Flow direction is from left to right.

Figure 28 displays the downstream component of bedload flux across each cross section where it was measured. In general, this also tracked the zone of maximum velocity and maximum boundary shear stress.
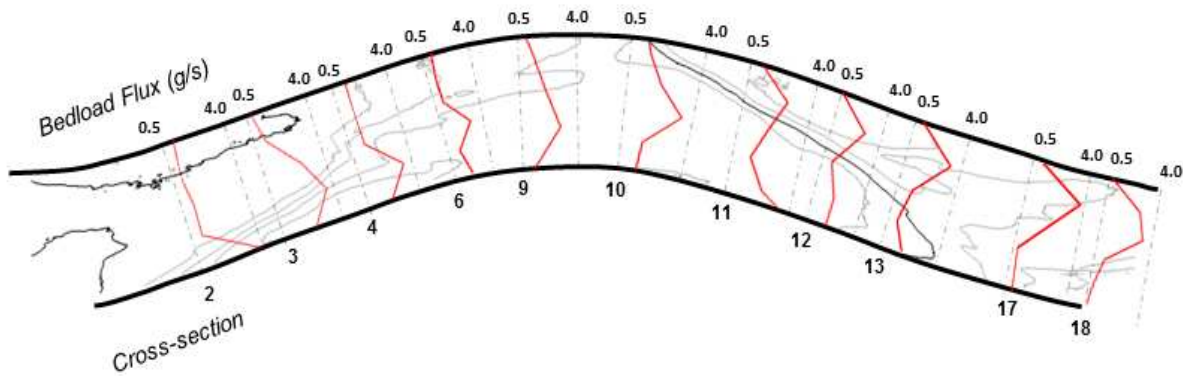
Figure 28. Downstream bedload flux profiles for each cross-section layered over bed topography contours. Flow direction is from left to right.

To further illustrate this, Figure 29 overlays the zone of maximum shear stress with the locus of maximum downstream bedload transport. There is generally a strong correspondence between the stress field and the sediment transport field.
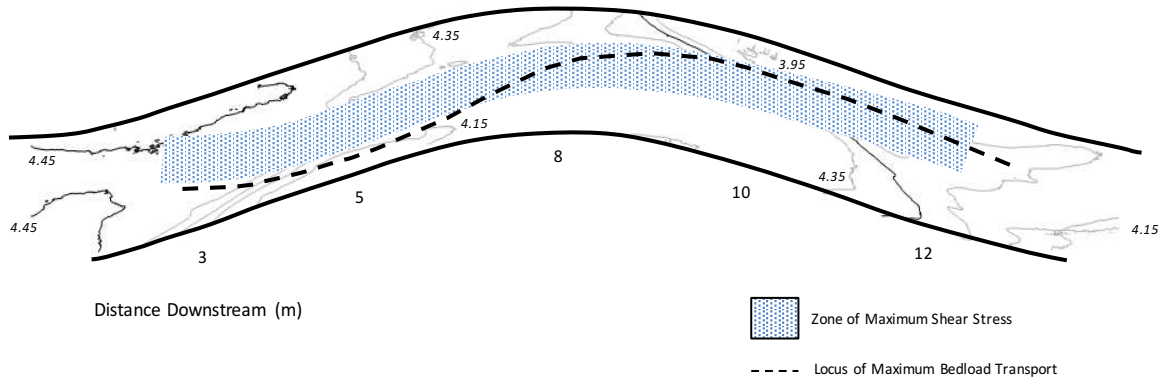
Figure 29. 20 degree bend showing the locus of maximum bedload transport for all grain size classes and the zone of maximum boundary stress stress.

The downstream sediment transport measurements were used to compute cross-stream sediment flux assuming steady state conditions. In this calculation, following Dietrich and Smith (1984) and Nelson et al. (2010), the downstream flux measurements were first corrected so that the corrected fluxes integrated across each cross section equaled the total downstream flux (Q_s) measured across all of the cross-sections (527.4 g/s). The resulting distributions of cross stream flux, q_n, are shown in Figure 30, and the ratio of the integrated cross stream flux (Q_n) to the average integrated downstream flux (Q_s) is shown in Figure 31. The average ratio Q_n/Q_s is 0.35, and negative values indicate net flux toward the right bank while positive values indicate net flux toward the left bank. In general, there tends to be net flux toward the right bank until about $s = 5$ m, then net flux toward the left bank until about $s = 10.5$ m, then net flux toward the right bank again until $s = 13$ m.
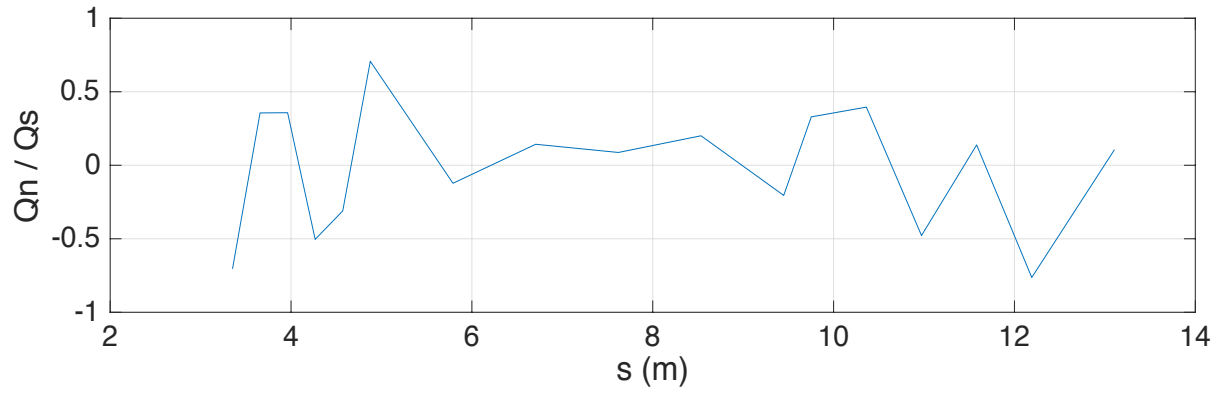
Figure 30. Ratio of total cross stream flux to total downstream sediment flux (Q_n/Q_s) at each cross section. Positive values indicate net flux toward the left bank, while negative values indicate net flux toward the right bank.
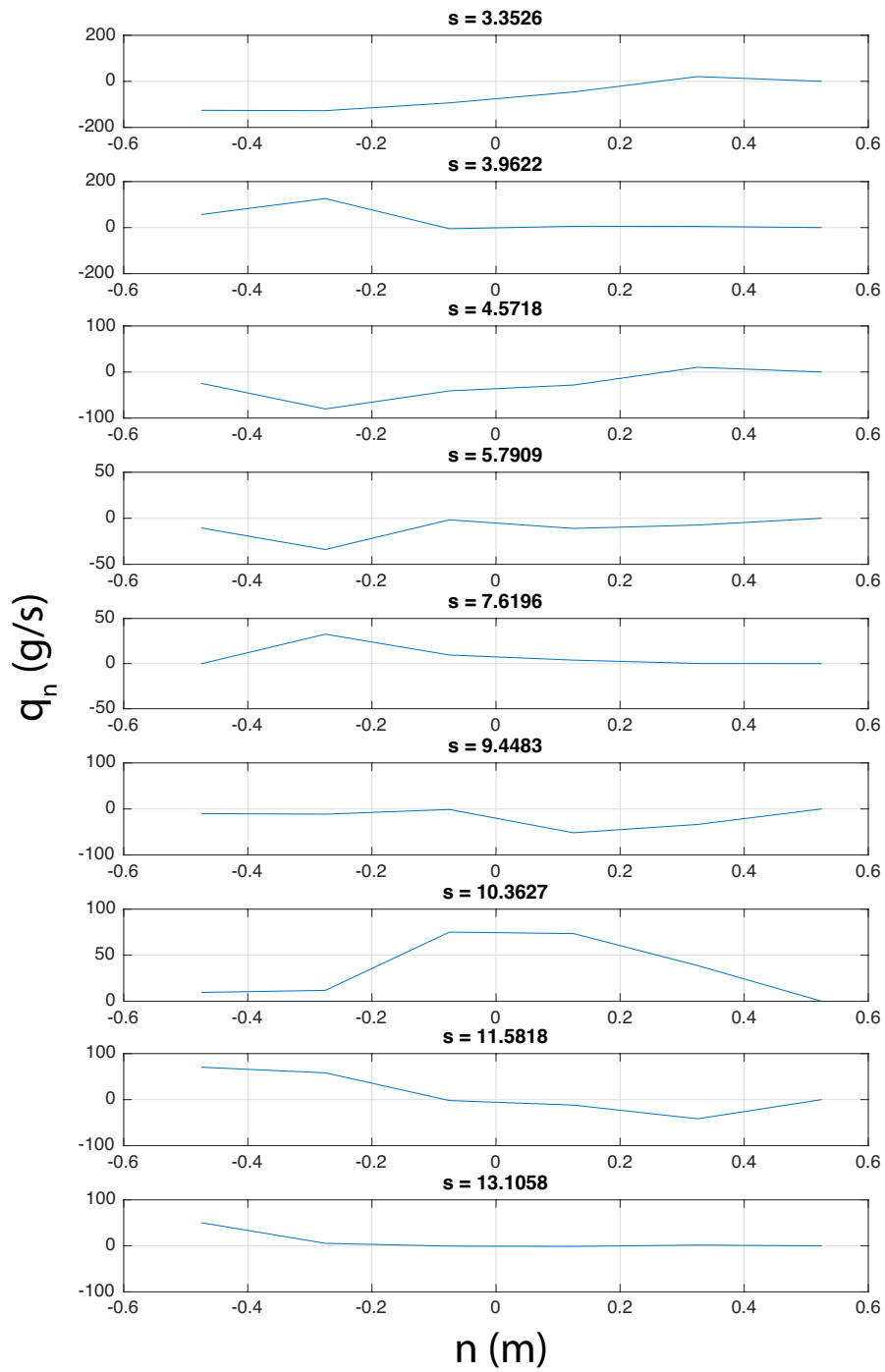
Figure 31. Cross-stream sediment flux (q_n) computed from downstream flux measurements under the steady-state assumption. Positive q_n values indicate flux toward the left bank, negative values indicate flux toward the right bank. The downstream location (s) (in meters) is given for each plot.

4. DISCUSSION

4.1 Free and forced bars

Forced bars were quick to develop in both Runs 2 and 3 (straight and meandering configurations), but the meandering configuration (20 degree crossing angle) took longer to reach equilibrium. The flow obstruction in Run 2 (straight channel configuration) was extremely effective in creating a forced pool and bar based on induced jet flow and eddies. This created the most stable bars and pools out of all of the simulations.

Interesting free bar or "lobe" behavior was observed over the long run duration (75 hours) in the straight channel in Run 1 (without an obstruction). The free bars exhibited "pulse-like" movements. Effort was made to track their migration over the entire length of the channel. Due to their (sometimes) ephemeral nature and tendency to converge or disappear, it was sometimes very difficult to parse out independent sediment pulses. The bars that remained separate entities were tracked over the course of approximately 20 hours. Structure from Motion (SfM) methods proved to be very helpful in tracking lobes. Most of the SfM scans were collected after the 30-hour mark and were taken 2 hours apart. In addition to SfM scans, drawings were made to track the head of the bar as it moved downstream. Migration patterns were mapped and migration rates calculated. Migration rates became fairly steady as equilibrium was reached (around 60 hours and beyond).

Despite the episodic and unstable nature of most of the free bars, two stable points were present during the entire simulation duration. Both features were located adjacent to either the upstream or downstream of the channel, including pieces of sheet metal that were installed at the upstream and downstream end of the flume to maintain a certain bed thickness and contain the

bed material. The meandering channel also featured free bars, however, as stated above, this behavior was ephemeral and activity tapered off as equilibrium was reached.

Comparing the topography achieved in the straight channels, it seems that the obstruction was crucial in achieving forced bars. The ability of obstructions to generate forced bars is well documented in the literature (Thompson and McCarrick, 2010). In addition, previous studies have shown the effectiveness of meandering channels in forcing bars, especially those with high width to depth ratios (Garcia and Nino, 1993; Whiting and Dietrich, 1993). Point bars in curved channels can suppress migrating bars, creating stable conditions (Tubino and Seminara, 1990; Whiting and Dietrich, 1993). Unlike both the straight channel (with the obstruction) and meandering channel, the channel without an obstruction never reached bar stability. In Lanzoni (2000), the formation of free bars in a straight channel was investigated. Transient bars were observed and these bars were described as "longitudinal alternate streaks of coarse and fine material," which often joined to form "incipient small bars." This description is very similar to what was observed in the straight channel. Lanzoni (2000) hypothesized that these patterns were triggered by random disturbances in the channel boundary conditions (i.e. flow or sediment supply) or fluctuations in the flow and sediment field caused by "poorly" developed bars located upstream. It is possible that the bars did not stabilize in the straight channel (with no obstruction) because a combination of these factors. The nature of the sediment supply may have attributed to the pulse-like behavior of the bars. In addition, small irregular bars were observed near the upstream end of the channel throughout the course of the experiment. These could have influenced the behavior and stability of downstream bars. It is also possible that the lack of forcing conditions (i.e. obstruction or curvature) attributed to the migration and absence of bar stability. Whiting and Dietrich (1993) reported that migration is low in channels with strong

shear stresses and sediment transport divergence. Though strong shear stresses were not observed in the meandering channel, sediment transport divergence was. This could have attributed to the further suppression of free bars and the trend towards stability in the 20 degree channel.

4.2. Shear stress, sediment transport, and sorting in gravel-bed meanders

Under equilibrium conditions, the curved channel in Run 3 developed a strongly heterogeneous boundary shear stress field. Our observations suggest that this shear stress divergence was almost entirely accommodated by cross-stream sediment transport, such that there is convergent transport into areas of increasing shear stress and divergent transport from areas of decreasing shear stress. While Dietrich and Smith (1984) found that the sand-bedded meander in Muddy Creek accommodated stress divergences with both sediment transport divergences and bed surface coarsening, the results from our gravel-bed flume experiment showed virtually no surface sorting.

This lack of sorting is rather surprising. It is possible that the bulk grain size distribution used in the experiments was too well sorted and with too narrow a grain size range to achieve distinct sorting patterns. This seems unlikely, however, given that other experiments have used quite similar grain size distributions and observed sorting features such as bed surface patches and bedload sheets (Dietrich et al., 1989; Nelson et al., 2009). A more likely explanation for the lack of sorting has to do with the nature of gravel transport. Gravel transport is generally considered to be nonlinearly proportional to the excess shear stress; that is, the amount by which the applied boundary shear stress exceeds the critical value for grain entrainment, commonly approximated by the critical Shields number:

$$\tau_c^* = \frac{\tau_c}{(\rho_s - \rho)gD_{50}}$$

Here, τ_c is the dimensional shear stress at which grains of size $D50$ will be entrained, ρ_s is

the density of sediment, ρ is the density of water, g is gravitational acceleration, and τ_c is the

critical dimensionless shear stress, also called the Shields number. The Shields number is often

approximated with empirical relationships, and in the gravel range a common critical value is τ_c^*

= 0.045. Using this approximation, and the bed surface D50 values shown in Figure 24 we can

plot the excess shear stress τ/τ_c for each of our cross sections, as shown in Figure 32.

Figure 32. Ratio of boundary shear stress (τ) to critical shear stress (τ_{crit}) profiles plotted for each cross-section layered over bed topography contours (showing the high and low points of interest). Flow direction is from left to right. Elevations (in meters) of key contours are given in italics.

The calculation error is associated with the velocity error (both measured height of the velocity

measurement and the measured point velocity itself), which is <0.003 m/s and 1 cm, and D50,

which was estimated to be approximately 2 mm.

Over nearly the entire bend, the shear stress is either below critical or just barely above

the critical value. With low stresses such as these, it may be that the cross-stream variation in

boundary shear stress above the critical value was not large enough to cause areas of the bed to

become coarse and immobile. With such low applied stress, it is possible that the increase in

local critical shear stress at locations that may have experienced coarsening would have

49

exceeded the applied stress and resulted in local deposition and fining, essentially creating a negative feedback that prevents strong sorting from happening. This also suggests that during the experiment, the bed as a whole was coarser than the sediment that was transported as bedload. This contrasts with sandy channels such as Muddy Creek, where even low flows can produce shear stresses far in excess what what is necessary to entrain sand.

And yet, despite the potential negative sorting feedback associated with low excess stress conditions typical of gravel bed channels, field observations of gravel-bed meanders still show strong sorting patterns (e.g., Clayton and Pitlick, 2008; Clayton, 2010). This suggests that conditions in nature not captured in our flume experiment play an important role in developing bed sorting in gravel bends. One likely possibility here is unsteady flow: in the field, as flows increase on the rising limb of a hydrograph, larger and larger grain sizes present on a gravel bed will become entrained as transport shifts from partial to selective to equal mobility. This may allow for gravitational effects and secondary circulations to have a stronger influence on the range of grain sizes being transported through bends, encouraging the development of bar-pool sorting patterns. Additionally, on the falling limb of the hydrograph, the size distribution of the bedload will continue to change as the shear stress declines, and the timing of when the transport rate of particles of different sizes declines dramatically will likely impart a signature on the pattern of grain sizes on the bed.

It is also possible that though there were not surface sorting patterns, there could have been subsurface sorting patterns that were not made evident by the surface observations. The high surface grain sizes observed in the curved channel could be attributed to surface coarsening within the channel and the creation of an armor layer. Subsurface measurements, however, were not collected, therefore only speculations can be made about the existence of coarsening. The

observed coarsening could also be credited to the measurement error associated with the automated photo analysis (estimated to be approximately 2 mm).

5. CONCLUSIONS

Meandering channels feature high degrees of channel complexity and natural dynamic channel stability. While extensive research has focused on secondary flow and sediment transport in curved channels, very little research has looked at the interaction between velocity, grain sorting, and meandering in mixed-grain gravel-bed channels. The initial objective of this study was to investigate the mechanisms responsible for sorting patterns in mixed-grain straight and curved channels. After a scarcity of sorting was observed in the flume experiments, the study objective shifted. The objective was modified to: 1) investigate the formation, behavior, and dynamics of free and forced bars within a straight channel with and without an upstream barrier and 2) explore the mechanism that accounts for spatial boundary shear stress variations in curved gravel bed channels. This study provided an extension of the work done by Dietrich and Smith (1989) and Nelson et al. (2010) by examining the relationship between flow, sediment transport, and bed topography in a meandering mixed-grain channel under equilibrium conditions. The flume setting provided conditions that were more stable and controlled than the meandering gravel bed channel in Dietrich and Smith (1989).

With regards to free and forced bar behavior, no stability was achieved in the straight channel without an obstruction. This could have occurred due to a wide variety of factors related to upstream boundary conditions, shear stress, and lack of forcing topography. Meanwhile, both the curved channel and straight channel (with an obstruction) achieved stability through the suppression of free bars and creation of conditions ideal for forced bars.

It was initially expected that the curved channel would feature strong sorting patterns (grain size adjustment) that would compensate for spatial variations in shear stress instead of

sediment transport divergence/convergence. However, these strong sorting patterns were not observed in the curved channel. The data reveal sediment transport divergence as the primary mechanism for balancing shear stress variability. The lack of sorting can likely be attributed to low excess shear stress. The shear stresses present were either below critical stress or barely above. In addition, the lack of strong surface sorting could be accredited to the absence of unsteady flow conditions, which in the field, create heterogeneous conditions necessary for sediment mobility (i.e. partial, selective, and equal) and bar-pool sorting patterns. I suggest that future studies utilize both higher excess shear stress and unsteady flow conditions in investigating shear stress variability in curved gravel bed channels. In addition, it is suggested that subsurface grain size measurements be collected to adequately capture subsurface sorting patterns (including surface coarsening).

REFERENCES

Bankert, A and Nelson, P.A. (In review). Alternate bar dynamics in response to increases and decreases of sediment supply, submitted to *Sedimentology*.

Blondeau, P. and Seminara, G. (1985). A unified bar-bend theory of river meanders. *Journal of Fluid Mechanics,* 157, 449-470.

Bluck, B. J. (1971). Sedimentation in the meandering River Endrick, Scott. *J. Geol*., 7, 93–138.

Bluck, B. J. (1987). Bed forms and clast size changes in gravel- bed rivers, in River Channels: Environment and Process. *Inst. Br. Geogr. Spec. Publ.,* 18, 159–178.

Bridge, J. S., and Jarvis, J. (1976), Flow and sedimentary processes in the meandering river South Esk, Glen Clova, Scotland. *Earth Surface Processes*, 1, 303–336.

Bridge, J. S., and Jarvis, J. (1982). The dynamics of a river bend: A study in flow and sedimentary processes. *Sedimentology*, 29(4), 499-541.

Carson, M. A. (1986), Characteristics of high- energy "meandering" rivers; the Canterbury Plains, New Zealand, Bull. *Mem. Geol. Soc. Am.*, 97(7), 886–895.

Clayton, J. A. (2010), Local sorting, bend curvature, and particle mobility in meandering gravel bed rivers. *Water Resources Research*., 46, W02601.

Clayton, J. A. and Pitlick, J. (2007). Spatial and temporal variations in bed load transport intensity in a gravel bed river bend. *Water Resources Research*, 43(2).

Clayton, J. A., and Pitlick, J. (2008), Persistence of the surface texture of a gravel- bed river during a large flood. *Earth Surface Processes Landforms*, 33(5), 661–673.

Colombini, M., Seminara, G., and Tubino, M. (1987). Finite- amplitude alternate bars. *J. Fluid Mech.,* 181, 213–232.

Dietrich, W. E., and Smith, J. D. (1983), Influence of the point bar on flow through curved channels. *Water Resources Research*, 19(5), 1173–1192.

Dietrich, W. E. and Smith, J.D. (1984). Bed load transport in a river meander. *Water Resources Research*, 20(10), 1355-1380.

Dietrich, W. E., and Whiting, P. (1989), Boundary shear stress and sediment transport in river meanders of sand and gravel, in River Meandering. *Water Resources Monogr*am, vol. 12, edited by S. Ikeda and G. Parker, pp. 1–50, AGU, Washington, D. C.

Fonstad, M.A., Dietrich, J.T., Courville, B.C., Jensen, J.L., and Carbonneau, P.E. (2013). Topographic structure from motion: A new development in photogrammetric measurement. *Earth Surface Processes and Landforms*, 38(4), 421-430.

Garcia, M. and Niño, Y. (1993). Dynamics of sediment bars in straight and meandering channels: experiments on the resonance phenomenon. *Journal of Hydraulic Research*, 31(6), 739-761.

Graham, D. J., Reid, I., and Rice, S. P. (2005), Automated sizing of coarse grained sediments: Image-processing procedures. *Math. Geol.*, 37(1), 1–28.

Ikeda, S. (1989). Sediment transport and sorting at bends. In S. Ikeda & G. Part (Eds.), *River Meandering American Geophysical Union Water Resources Monograph*. (pp. 103-25). Washington, DC: American Geophysical Union.

Ikeda, S., Parker, G., and Sawai, K. (1981). Bend theory of river meanders. Part 1. Linear development. *Journal of Fluid Mechanics.*, 112, 363-377.

Johannesson, H. and Parker, G. (1989). Linear theory of river meanders. In S. Ikeda & G. Parker (Eds.), *River Meandering American Geophysical Union Water Resources Monograph*. (pp. 181-212). Washington, DC: American Geophysical Union.

Kinerson, D. (1990), Surface response to sediment supply, M.S. thesis, Univ. of Calif., Berkeley.

Kinoshita, R. and Miwa, H. (1974). River channel formation which prevents downstream translation of transverse bars. *Shinsabo*, 94, 12-17.

Langbein, W. B. and Leopold, L.B. (1966). *River meanders-theory of minimum variance*. US Government Printing Office.

Lanzoni, S. (2000). Experiments on bar formation in a straight flume. *Journal of Fluid Mechanics*, 393, 149-174.

Laronne, J., and M. Duncan (1992). Bedload transport paths and gravel bar formation. *Dynamics of Gravel- bed Rivers*, 177–202.

Lisle, T. E., and Hilton, S. (1992), Volume of fine sediment in pools: An index of sediment supply in gravel- bed streams. *Water Resources Bulletin*, 28(2), 371–383.

Lisle, T., and Madej, M. (1992). Spatial variation in armouring in a channel with high sediment supply. *Dynamics of Gravel- bed Rivers*, 277–293.

Morgan, J., Brogan, D., and Nelson, P.A. (2016). Application of structure-from-motion to laboratory flumes. *Geomorphology*, 276, 125-143.

Mosley, M. P., and Tindale, D. S. (1985), Sediment variability and bed material sampling in gravel- bed rivers. *Earth Surfaces Processes Landforms*, 10(5), 465–482.

Nelson, P. A., Venditti, J. G., Dietrich, W. E., Kirchner, J. W., Ikeda, H., Iseya, F., and Sklar, L. S. (2009). Response of bed surface patchiness to reductions in sediment supply, *Journal of Geophysical Research*, 114, F02005.

Nelson, P. A., Dietrich, W. E., and Venditti, J.G. (2010). Bed topography and the development of forced bed surface patches. *Journal of Geophysical Research,* 115.

Nelson, P. A., Mcdonald, R. R., Nelson, J.M., and Dietrich, W. E. (2015a). Coevolution of bed surface patchiness and channel morphology: 1. Mechanisms of forced patch formation." *Journal of Geophysical Research*, 120(9), 1687-1707.

Nelson, P. A., Mcdonald, R. R., Nelson, J. M., and Dietrich, W. E. (2015b). Coevolution of bed surface patchiness and channel morphology: 2. Numerical experiments." *Journal of Geophysical Research*, 120(9), 1708-1723.

Parker, Gary and Andrews, E.D. (1985). Sorting of bed load sediment by flow in meander bends. *Water Resources Research*, 21(9), 1361-1373.

Seminara, G. (2006). "Meanders." *Journal of Fluid Mechanics*, 554, 271-297.

Seminara, G., and L. Solari (1998). Finite amplitude bed deformations in totally and partially transporting wide channel bends, *Water Resources Research*, 34(6), 1585–1598.

Thompson, D.M. and McCarrick, C.R. (2010). A flume experiment on the effect of constriction shape on the formation of forced pools. *Hydrology and Earth System Sciences,* 14, 1321-1330.

Tubino, M. and Seminara, G. (1990). Free–forced interactions in developing meanders and suppression of free bars. *Journal of Fluid Mechanics,* 214, 131-159.

Venditti, J. G., Nelson, P. A., Minear, J. T., Wooster, J., and Dietrich, W. E. (2012). Alternate bar response to sediment supply termination." *Journal of Geophysical Research*.

Westoby, M.J., Brasington, J. , Glasser, Hambrey M.J., and Reynolds, J.M. (2012). 'Structure-from-motion' photogrammetry: A low-cost, effective tool for geoscience applications." *Geomorphology*, 179, 300-314.

Whiting, Peter J., and Dietrich, W. E. (1993). "Experimental constraints on bar migration through bends: Implications for meander wavelength selection." *Water Resources Research,* 29(4), 1091-1102.

Wilcock, P. R., and Crowe, J. C. (2003), Surface- based transport model for mixed-size sediment, *Journal of Hydraulic Engineering,* 129(2), 120–128.

Wilcock, P.R. and McArdell, B.W. (1993). Surface-based fractional transport rates: mobilization thresholds and partial transport of a sand-gravel sediment. *Water Resources Research*, 29(4), 1297-1312.